



Calhoun: The NPS Institutional Archive
DSpace Repository

Theses and Dissertations

1. Thesis and Dissertation Collection, all items

2004-12

High responsivity tunable step quantum well infrared photodetector

Yeo, Hwee Tiong

Monterey, California. Naval Postgraduate School

<http://hdl.handle.net/10945/1294>

Copyright is reserved by the copyright owner

Downloaded from NPS Archive: Calhoun



Calhoun is the Naval Postgraduate School's public access digital repository for research materials and institutional publications created by the NPS community. Calhoun is named for Professor of Mathematics Guy K. Calhoun, NPS's first appointed -- and published -- scholarly author.

Dudley Knox Library / Naval Postgraduate School
411 Dyer Road / 1 University Circle
Monterey, California USA 93943

<http://www.nps.edu/library>



NAVAL POSTGRADUATE SCHOOL

MONTEREY, CALIFORNIA

THESIS

**HIGH RESPONSIVITY TUNABLE STEP QUANTUM
WELL INFRARED PHOTODETECTOR**

by

Yeo Hwee Tiong

December 2004

Thesis Advisor:
Second Reader:

Gamani Karunasiri
James Luscombe

Approved for public release; distribution is unlimited.

THIS PAGE INTENTIONALLY LEFT BLANK

REPORT DOCUMENTATION PAGE			<i>Form Approved OMB No. 0704-0188</i>	
Public reporting burden for this collection of information is estimated to average 1 hour per response, including the time for reviewing instruction, searching existing data sources, gathering and maintaining the data needed, and completing and reviewing the collection of information. Send comments regarding this burden estimate or any other aspect of this collection of information, including suggestions for reducing this burden, to Washington headquarters Services, Directorate for Information Operations and Reports, 1215 Jefferson Davis Highway, Suite 1204, Arlington, VA 22202-4302, and to the Office of Management and Budget, Paperwork Reduction Project (0704-0188) Washington DC 20503.				
1. AGENCY USE ONLY (Leave blank)		2. REPORT DATE December 2004	3. REPORT TYPE AND DATES COVERED Master's Thesis	
4. TITLE AND SUBTITLE High Responsivity Tunable Step Quantum Well Infrared Photodetector.			5. FUNDING NUMBERS	
6. AUTHOR(S) Yeo Hwee Tiong				
7. PERFORMING ORGANIZATION NAME(S) AND ADDRESS(ES) Naval Postgraduate School Monterey, CA 93943-5000			8. PERFORMING ORGANIZATION REPORT NUMBER	
9. SPONSORING /MONITORING AGENCY NAME(S) AND ADDRESS(ES) N/A			10. SPONSORING/MONITORING AGENCY REPORT NUMBER	
11. SUPPLEMENTARY NOTES The views expressed in this thesis are those of the author and do not reflect the official policy or position of the Department of Defense or the U.S. Government.				
12a. DISTRIBUTION / AVAILABILITY STATEMENT Approved for public release; distribution is unlimited.			12b. DISTRIBUTION CODE	
13. ABSTRACT (maximum 200 words) <p>In this thesis, the performance of a step quantum well infrared photodetector (QWIP), which was designed to detect a laser spot at $1.05 \mu m$ and IR radiation between $9.5 \mu m$ to $10.5 \mu m$, was evaluated. In the far infrared (FIR), the maximum responsivity of the test detector at 10 K was measured at 1.02 A/W with a peak wavelength of $10.3 \mu m$ under a negative bias of 0.83 V. The D^* at background limited infrared performance (BLIP) was measured at $8.0 \times 10^9 cm \sqrt{Hz} / W$ with 180° field of view. The BLIP temperature was found to be about 55 K. In addition, the FIR detection wavelength found shift with the amount of bias across the device. The amount of shift observed was $0.21 meV/KVcm^{-1}$ which is due to linear Stark effect associated with the step quantum well. The quantum well infrared detectors made of square quantum wells found to have an order of magnitude lower Stark shift originated from second order effects. This suggests that the step well infrared detector can have applications in tunable wavelength infrared detectors.</p>				
14. SUBJECT TERMS Asymmetric Quantum Well, Step Quantum Well Infrared Photodetector, Stark Effect.			15. NUMBER OF PAGES 81	
			16. PRICE CODE	
17. SECURITY CLASSIFICATION OF REPORT Unclassified	18. SECURITY CLASSIFICATION OF THIS PAGE Unclassified	19. SECURITY CLASSIFICATION OF ABSTRACT Unclassified	20. LIMITATION OF ABSTRACT UL	

NSN 7540-01-280-5500

Standard Form 298 (Rev. 2-89)
Prescribed by ANSI Std. Z39-18

THIS PAGE INTENTIONALLY LEFT BLANK

Approved for public release; distribution is unlimited.

**HIGH RESPONSIVITY TUNABLE STEP QUANTUM WELL INFRARED
PHOTODETECTOR**

Hwee T Yeo
Major, Republic of Singapore Navy
B.E. (Electrical), National University of Singapore, 1997

Submitted in partial fulfillment of the
requirements for the degree of

MASTER OF SCIENCE IN APPLIED PHYSICS

from the

**NAVAL POSTGRADUATE SCHOOL
December 2004**

Author: Hwee Tiong, Yeo

Approved by: Gamani Karunasiri
Thesis Advisor

James Luscombe
Second Reader

James Luscombe
Chairman, Department of Physics

THIS PAGE INTENTIONALLY LEFT BLANK

ABSTRACT

In this thesis, the performance of a step quantum well infrared photodetector (QWIP), which was designed to detect a laser spot at $1.05\ \mu m$ and IR radiation between $9.5\ \mu m$ to $10.5\ \mu m$, was evaluated. In the far infrared (FIR), the maximum responsivity of the test detector at 10 K was measured at 1.02 A/W with a peak wavelength of $10.3\ \mu m$ under a negative bias of 0.83 V. The D^* at background limited infrared performance (BLIP) was measured at $8.0 \times 10^9\ cm\sqrt{Hz}/W$ with 180° field of view. The BLIP temperature was found to be about 55 K. In addition, the FIR detection wavelength found shift with the amount of bias across the device. The amount of shift observed was $0.21\ meV/KVcm^{-1}$ which is due to linear Stark effect associated with the step quantum well. The quantum well infrared detectors made of square quantum wells found to have an order of magnitude lower Stark shift originated from second order effects. This suggests that the step well infrared detector can have applications in tunable wavelength infrared detectors.

THIS PAGE INTENTIONALLY LEFT BLANK

TABLE OF CONTENTS

I.	INTRODUCTION.....	1
A.	QUANTUM WELL INFRARED PHOTODETECTORS (QWIP).....	1
B.	DEVELOPMENTS IN STEP QUANTUM WELL.....	7
C.	PURPOSE OF THIS THESIS.....	10
D.	MILITARY RELEVANCE	11
II.	QWIP BACKGROUND AND THEORY.....	13
A.	SQUARE QUANTUM WELLS	13
B.	TYPES OF QWIPS.....	15
1.	Bound-to-Bound QWIPs.....	15
2.	Bound-to-Continuum QWIPs	15
3.	Bound-to-Quasibound QWIPs	16
C.	TRANSITION RATE AND OSCILLATOR STRENGTH	17
D.	TUNING OF WAVELENGTH USING STARK EFFECT.....	19
III.	STEP QUANTUM WELL STRUCTURE	23
A.	SELECTION OF MATERIALS FOR QWIP	23
B.	FABRICATED STEP QWIP TEST DETECTOR	25
C.	ABSORPTION USING 45° FACET WAVEGUIDE.....	27
IV.	EXPERIMENTAL SETUP AND RESULTS ANALYSIS.....	29
A.	PHOTODETECTOR CHARACTERIZATION SYSTEM	29
B.	DEVICE PIN DIAGRAM.....	32
C.	CALCULATION OF RESPONSIVITY	35
D.	MEASUREMENT OF RESPONSIVITY	37
1.	Bias Dependence of Responsivity	37
2.	Stark Effect.....	40
3.	Temperature Dependence of Responsivity	44
4.	IV Characteristics and Dark Current Measurement	46
E.	DETECTIVITY	51
V.	CONCLUSION.....	55
	APPENDIX A : PICTURES OF THE JUNCTION BOX AND ROTATING MIRRORS	57
	APPENDIX B : SPECIFICATION SHEETS.....	59
	LIST OF REFERENCES.....	61
	INITIAL DISTRIBUTION LIST	65

THIS PAGE INTENTIONALLY LEFT BLANK

LIST OF FIGURES

Figure 1.	Infrared Spectrum.....	2
Figure 2.	Applications of Infrared System.....	3
Figure 3.	Detectivity of Cooled and Uncooled Detectors	4
Figure 4.	Photo-detection by semiconductor.	5
Figure 5.	Band Structure of a Quantum Well.....	6
Figure 6.	Bandgaps and Lattice Constants for Various III-V Alloys	7
Figure 7.	Square Quantum Well of AlGaAs and GaAs.	13
Figure 8.	(a) Bound-to-Bound, (b) Bound-to-Continuum and, (c) Bound-to-quasibound QWIPs.....	16
Figure 9.	45° Facet Geometry to Overcome Polarization Selection Rule.	18
Figure 10.	Diffraction Grating for Coupling of IR Radiation.....	19
Figure 11.	Linear Stark Effect in a Step Quantum Well.	21
Figure 12.	Diagram of Bandgap vs Lattice Constant for Different Materials	24
Figure 13.	Schematic Diagram for Structure of Fabricated Test Detector.	26
Figure 14.	Asymmetric Step QWIP Structure with Energy Levels.	27
Figure 15.	Dimensions of 45° Angled Facet Geometry Waveguide.....	28
Figure 16.	Characterization System Module 1: IR Sources and Monochromator.	29
Figure 17.	Characterization System Module 2: Mirror Configurations Directing IR Rays to Test and Reference Detectors.	30
Figure 18.	Charaterization System Module 3: Chopper Control and Lock-in Amplifiers for Monitoring Test and Reference Detector Outputs.	30
Figure 19.	Picture of Test Detector Showing Wire Bonding.....	33
Figure 20.	Schematic Diagram of the Test Detectors Wired to the Package for Manipulations and Measurements.....	34
Figure 21.	Responsivity as a function of wavelength at T = 10 K for a set of bias voltages.	38
Figure 22.	Conduction Band Structure and Electrons Transport (a) Under Negative Bias and (b) Under Positive Bias.....	40
Figure 23.	Normalized Responsivities Showing Stark Effect.	41
Figure 24.	Plots of Measured and Predicted Stark Shifts vs Electric Field.	43
Figure 25.	Responsivity at -0.15V Voltage Across the Detector for Different Temperatures.	44
Figure 26.	Responsivity at +0.15V Voltage Across the Detector for Different Temperatures.	45
Figure 27.	I-V Characteristics of Test Detector for Different Temperatures.....	47
Figure 28.	Dark Current Measurement.	48
Figure 29.	Periodic Dark Currents at Low Temperatures.	49
Figure 30.	Periodic Variation of Dark Current due to Sequential Resonant Tunneling.....	50

Figure 31. Detectivity (BLIP) of the Test Detector Under Different Bias Conditions.	53
--	----

LIST OF TABLES

Table 1.	Stark Shifts Observed for LOG Transition for Different Well Structures	9
Table 2.	Details of Wafer Specifications.....	26
Table 3.	Measured Energy Shifts due to Stark Effect for Different Electric Fields.....	43

THIS PAGE INTENTIONALLY LEFT BLANK

ACKNOWLEDGMENTS

I would like to express my appreciation to Professor Gamani Karunasiri, for the guidance and help he had given me, which were vital to the completion of this thesis. He had always been friendly and patient, taking time to explain and engage in fruitful discussions.

I would also like to thank my wife and daughter, who have really made my experience in the Naval Postgraduate School an even more fulfilling one.

THIS PAGE INTENTIONALLY LEFT BLANK

I. INTRODUCTION

A. QUANTUM WELL INFRARED PHOTODETECTORS (QWIP)

Infrared imaging systems have been and will continue to be a key differentiating factor in today's highly sophisticated battlefields (Sarusi, 2003). The large variety of military applications that employed infrared imaging systems is the principal driving force behind the development of new generation techniques and devices as well as the search for new alternatives for existing infrared systems. Some of these applications include ground-based, space-based surveillance and targeting systems, weapon night sights, aircraft fire-control systems and weapon-seeker systems.

The infrared spectrum can be broadly divided in to three bands as shown in Figure 1. The Near Infrared (NIR) covering wavelengths from $0.8\ \mu m$ to $3\ \mu m$, the Middle Infrared (MIR) covering wavelengths from $3\ \mu m$ to $6\ \mu m$, while the Far Infrared (FIR) covering wavelengths from $6\ \mu m$ to $15\ \mu m$. The bottom of Figure 1 also shows the major absorption components in the atmosphere which led to the three atmospheric windows in the visible, and the MIR window of $3\ \mu m$ to $5\ \mu m$ and FIR window of $8\ \mu m$ to $14\ \mu m$ which are commonly used in thermal imaging systems.

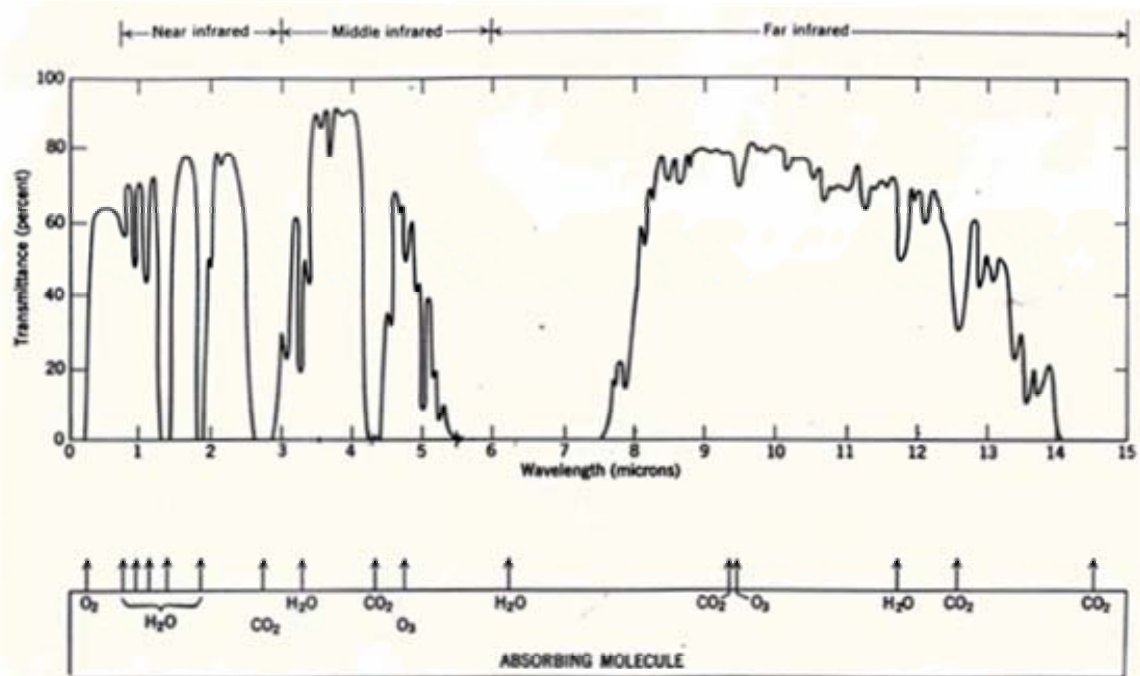


Figure 1 Transmittance of the atmosphere for a 6000 ft horizontal path at sea level

Figure 1. Infrared Spectrum.
([From Dereniak, et al, 1996, pp 34]).

Figure 2 shows a table categorizing the different level of applications and the general trend of development for thermal imaging systems. The main materials used for infrared detectors throughout the last three decades were mercury cadmium telluride (HgCdTe or MCT), indium antimonide (InSb) and platinum silicide (PtSi). Although these materials have been popular choices due to their unique properties, there were also associated challenges in using them. Particularly, some of these challenges include the lack of uniformity in the materials, which is a key requirement in building large format focal plane arrays (FPAs), especially in FIR applications in the 8-12 μm window. In addition, material defects and surface problems in these materials also led to degrading performances. Most of these problems are associated with the small bandgap and exotic nature of these materials.

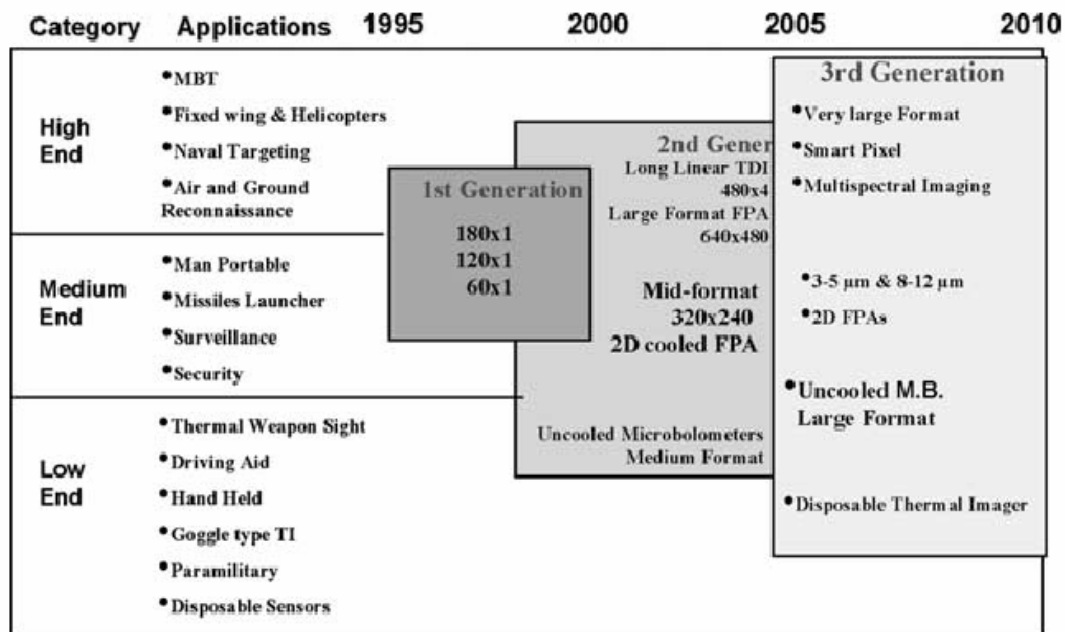


Figure 2. Applications of Infrared System.
([From Sarusi, 2003]).

Although technologies based on uncooled microbolometers have since emerged, their potential is still limited to those low-end to mid-end applications due to their limited performance. This is evident in the detectivity plots comparing cooled and uncooled detectors shown in Figure 3. It can be seen that there is a two orders of magnitude difference in the detectivities achievable between cooled and uncooled infrared detector systems.

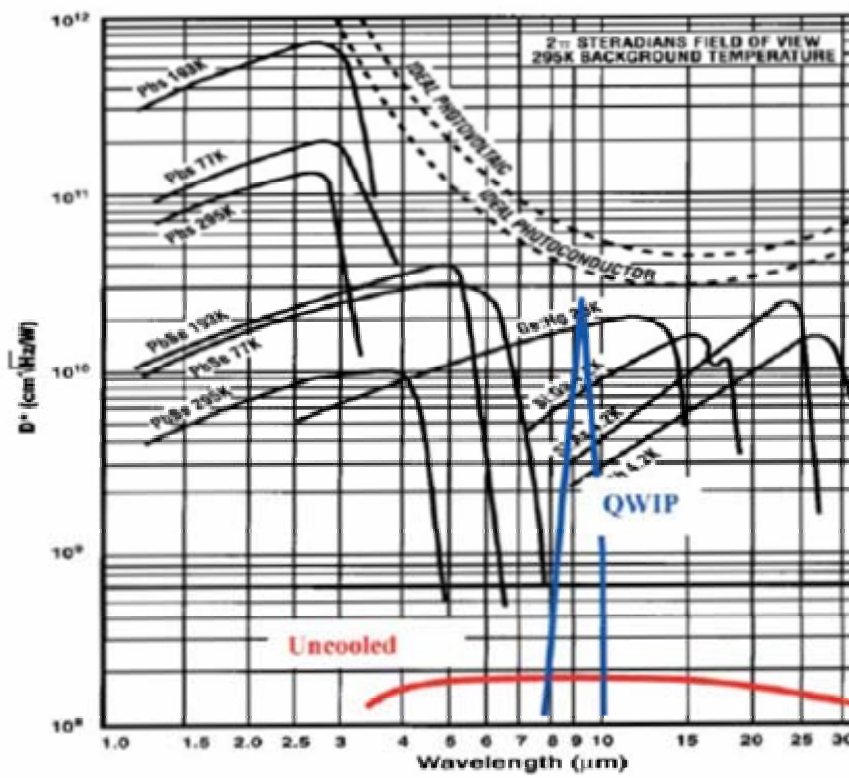


Figure 3. Detectivity of Cooled and Uncooled Detectors ([From Sarusi, 2003]).

In conventional photodetectors, the optical interband absorption involves exciting electron across the band gap E_g from the valence band to the conduction band as schematically shown in Figure 4. Radiation with energies larger than the bandgap will be absorbed while those less than the bandgap will pass through the detector in a transparent manner. The cutoff wavelength (λ_g) can be easily obtained from the bandgap via eq. (1.1), (Kasap, 2001).

$$\lambda_g(\mu m) = \frac{1.24}{E_g(eV)} \quad (1.1)$$

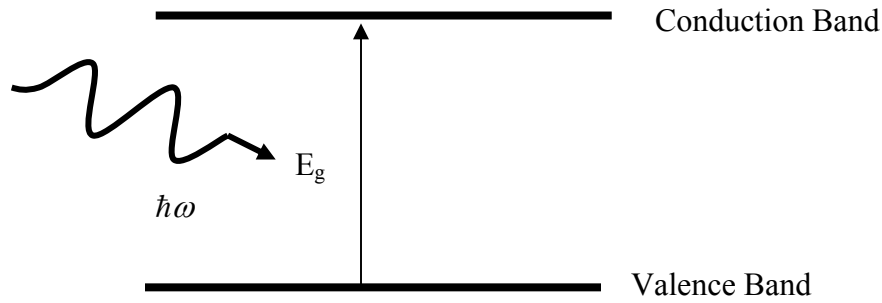


Figure 4. Photo-detection by semiconductor.

Only photon of wavelengths below a certain cutoff wavelength will be detected. By choosing different semiconductor materials, the bandgaps can be varied and thereby modifying the wavelength dependence of the detector response. However, as eq. (1.1) implies, detection of long wavelength radiation requires small bandgaps, and small bandgap materials are known to be more difficult to fabricate and process than the large bandgap materials. Typically, MCT has been used for the 8-12 μm FIR window, while InSb has been the common material used for the 3-5 μm MIR window. However, as stated before, materials processing and defects have been the major challenges in producing large focal plane arrays.

One approach to overcome above material and processing issues is to employ intersubband transitions in quantum wells made of large bandgap materials such as GaAs/AlGaAs as illustrated in Figure 5 (Levine, 1993). These detectors are generally known as quantum well infrared photodetectors or QWIP. The quantum wells have to be doped since only the thermally excited electrons are occupied in the conduction band of undoped material which is far too small to have significant intersubband absorption. For example, a simple quantum well can be created by separating two regions of large band gap GaAs by a region of smaller bandgap InGaAs. The well structure enables energy spacing between the energy states within the well to become significant compared to the thermal energy such that optical transitions between states can be observed (Haegel, 2001). As shown in Figure 5, the working of QWIP involved the excitation of the

photocarriers so that they can escape from the well and be collected in the form of photocurrent.

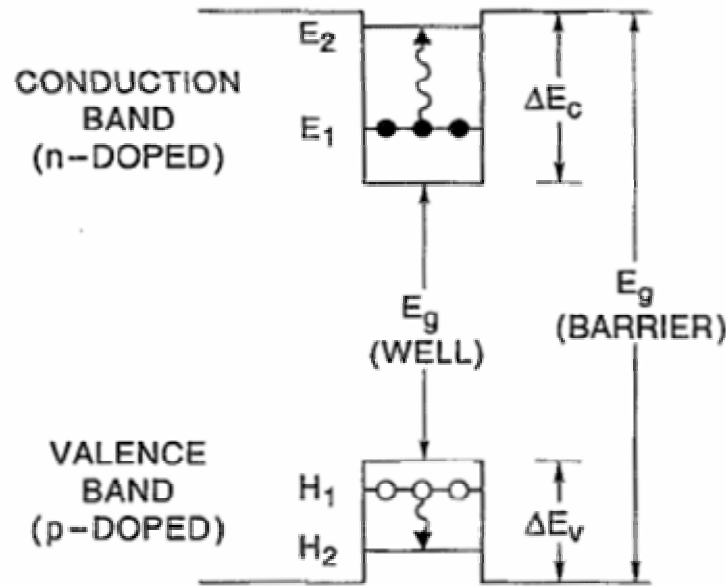


Figure 5. Band Structure of a Quantum Well.
([From Levine, 1993, pp R3]).

Referring to Figure 6, which is a common plot used for fabricating semiconductors heterostructures, by varying the amount of indium in InGaAs, the bandgap can be changed and hence the depth of the potential well can be altered, thereby allowing engineering of the wavelength responses. It was in 1985 that West and Eglash observed strong intersubband transition that triggered the birth of a large variety of QWIP devices thereafter (Levine, 1993). Our interest in this study is on the use of an asymmetric quantum well for fabrication of QWIP detector. Unlike traditional square quantum wells which do not show much shift in the peak wavelengths when different levels of bias or fields are applied to facilitate the collection of the photocurrent, an asymmetric step quantum well exhibits a considerable amount of shift as a result of the linear Stark effect (Yuh, 1989). The resultant tunability not only enhances the

operability of this type detector, but also presents additional options for other applications.

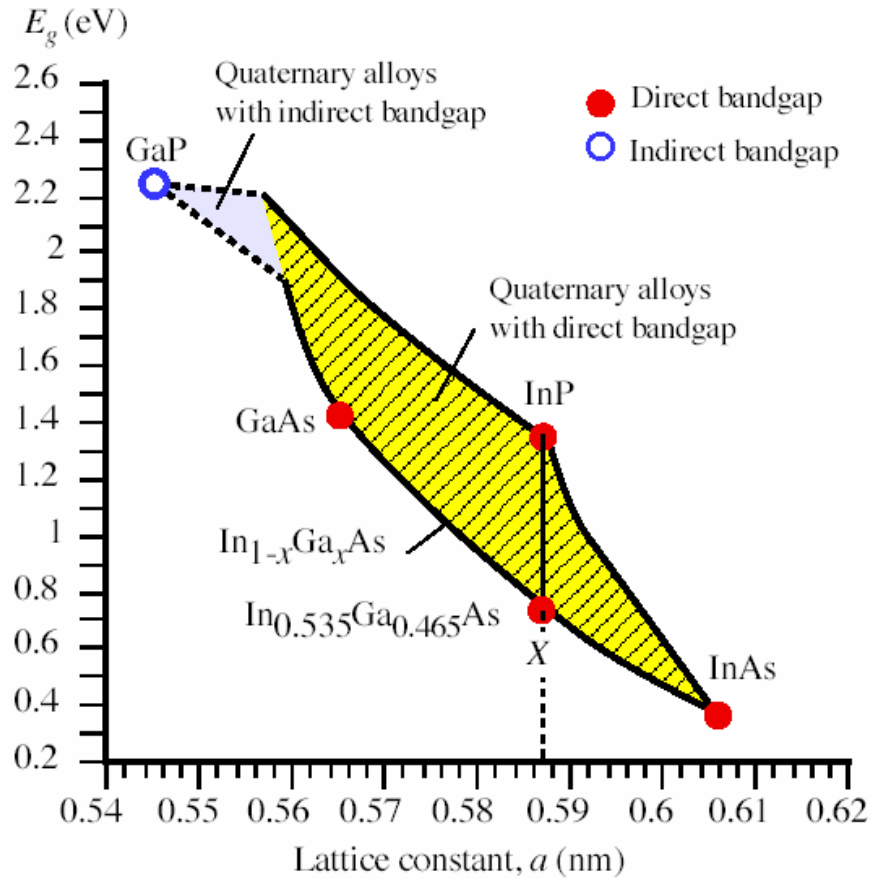


Figure 6. Bandgaps and Lattice Constants for Various III-V Alloys ([From Kasap, 2001, pp 155]).

B. DEVELOPMENTS IN STEP QUANTUM WELL

In 1987, Harwitt and Harris first observed Stark shifts in the intersubband transitions of common square well system and supported their measurements with theoretical analysis (Harwitt, et al, 1987). However, the effective stark shift of $0.02 \text{ meV/KVcm}^{-1}$ was relatively small and the need for a large electric field may

lead to excessive leakage currents in practical applications. Alternative structure in coupled quantum wells though yielding large shifts were accompanied by poor oscillator strengths since the shifts are caused by “interwell” types of transitions (Yuh, et al, 1989). Since the observation of optical transitions from the local states in the small well to the global states of the big well of a step quantum well which were accompanied by large shifts and the retention of large oscillator strengths (Yuh, et al, 1989), there have been significant efforts channeled into the development and study of this new structure, providing a strong alternative to the typical square quantum well. Table 1 shows a summary of stark shifts as well as oscillator strengths for several well structures based on the $\text{Al}_x\text{Ga}_{1-x}\text{As}/\text{GaAs}$ heterosystem (Yuh, et al, 1989). The first structure was a step well, the second, third, fourth, fifth, sixth and eighth were double coupled wells, and the seventh was a triple coupled wells. In short, it was observed that the step well measured a large stark shift while retaining good oscillator strength. When the number wells were increased, the oscillator strengths became smaller.

SUMMARY OF LOG TRANSITIONS FOR SEVERAL STRUCTURES. THE TRANSITION ENERGY (E) AND OSCILLATOR STRENGTH (OS) OR OVERLAP INTEGRAL (OI) ARE CALCULATED FOR FLATBAND CONDITION ($F = 0$) AND UNDER AN APPLIED FIELD 30 kV/cm ($F = 30$ kV/cm), RESPECTIVELY

Structures	Transition Type	Initial State	$F = 0$	$F = 30$ kV/cm	Stark Shift
37 _{0,2} 26 ₀	$1_c \rightarrow 2_c$ intersubband	47.4 meV	$E = 0.1156$ eV $OS = 0.65$ transparent	$E = 0.1257$ eV $OS = 0.81$ opaque	10.1 meV blue shift
26 ₀ 30 _{0,1} 26 ₀	$1_c \rightarrow 4_c$ intersubband	37.7 meV	$E = 0.1242$ eV $OS = 0.54$ opaque	$E = 0.1426$ eV $OS = 0.24$ transparent	18.4 meV blue shift
23 ₀ 20 _{0,2} 23 ₀	$2_c \rightarrow 3_c$ intersubband	58.4 meV	$E = 0.1234$ eV $OS = 1.14$ opaque	$E = 0.1068$ eV $OS = 0.50$ transparent	16.6 meV red shift
27 ₀ 17 _{0,2} 27 ₀	$1_c \rightarrow 3_c$ intersubband	42.4 meV	$E = 0.1141$ eV $OS = 0$ transparent	$E = 0.1237$ eV $OS = 0.75$ opaque	9.6 meV blue shift
23 ₀ 21 _{0,15} 23 ₀	$1_c \rightarrow 3_c$ intersubband	48.4 meV	$E = 0.1119$ eV $OS = 0$ transparent	$E = 0.1229$ eV $OS = 0.48$ opaque	11.0 meV blue shift
29 ₀ 22 _{0,15} 29 ₀	$1_c \rightarrow 4_c$ intersubband	36.7 meV	$E = 0.1248$ eV $OS = 0.66$ opaque	$E = 0.1477$ eV $OS = 0.12$ transparent	22.9 meV blue shift
25 ₀ 20 _{0,2} 25 ₀ 20 _{0,2} 25 ₀	$1_c \rightarrow 4_c$ intersubband	41.4 meV	$E = 0.1045$ eV $OS = 0.54$ transparent	$E = 0.1250$ eV $OS = 0.47$ opaque	20.5 meV blue shift
11 ₀ 35 _{0,1} 11 ₀	$1_h \rightarrow 1_c$ interband		$E = 1.608$ eV $OI = 0.78$ transparent	$E = 1.585$ eV $OI = 0.22$ opaque	16 meV red shift

Table 1. Stark Shifts Observed for LOG Transition for Different Well Structures ([From Yuh, et al, 1989]).

Following this, one of the largest Stark shifts from the LOG intersubband transition for a step well was measured at $0.44 \text{ meV/KVcm}^{-1}$ by Mii, et al (Mii, et al, 1990). Due to the extremely fast intersubband relaxation times of the order of 10 ps, one of the major potential applications was in high speed optical modulator applications such as for CO₂ lasers. This was successfully demonstrated when Karunasiri, et al, achieved strong modulation of the transmission of CO₂ laser beam (Karunasiri, et al, 1990). More alternative applications for the step well continued to emerge and one of them was the switchable bicolor IR detector by Martinet, et al. The group showed that by varying the applied electric field across the step well, the photo response could be switched between $5.5 \mu\text{m}$ and $9.0 \mu\text{m}$. The requirement for high electric field to achieve tunneling for the bound to bound transition however meant that moderate responsivities of 0.06 A/W and 0.12 A/W were achieved (Martinet, et

al, 1992). Continued works on two-color infrared detection was done by Mei, et al, with superlattice barriers at relatively low electric fields to reduce the dark currents employing bound-to-bound as well as bound-to-continuum transitions. Due to non optimized structure however, the maximum responsivity achieved was 4 mA/W, while the detectivities were estimated at $1.8 \times 10^9 \text{ cm(Hz)}^{1/2}/\text{W}$ and $1 \times 10^9 \text{ cm(Hz)}^{1/2}/\text{W}$ for the long and short wavelengths detections. Further optimization of the step well structure was done by Wu, et al, for the middle wavelength IR detectors in 2001. The group managed to achieve blackbody (500K) detectivity of $1 \times 10^{10} \text{ cm(Hz)}^{1/2}/\text{W}$ for the 3 to $5.3 \mu\text{m}$ IR atmospheric window (Wu, et al, 2001). Bias induced tuning as a result of the linear stark effect present in step quantum well was a common feature in all these results.

C. PURPOSE OF THIS THESIS

The purpose of this thesis is to evaluate and study the performance of an asymmetric quantum well infrared photodetector. The photodetector to be studied is that designed and fabricated in an earlier thesis (Touse, 2003). The design was based on a selected band structure for absorption of wavelengths near $1 \mu\text{m}$ and between $8 \mu\text{m}$ to $10 \mu\text{m}$ through the employment of both interband and intersubband absorptions. The focus of this thesis is to study the long wavelength response of the detector and the impact on the wavelength responses under different external bias as a result of Stark effect. The performance of the detector under different temperature conditions will also be evaluated. The photoresponse will be measured using a photodetector characterization system set up in a previous thesis (Herdlick, 2002). In addition, the current versus voltage characteristics will also be measured using a HP semiconductor analyzer so as to establish the dark current characteristics as well as the background limited performances.

D. MILITARY RELEVANCE

As mentioned above, the development of QWIPs is driven to a large extent by the diverse fields of applications in military thermal imaging system. The original intent for the energy band structure design was to achieve a multicolor QWIP that can be used as both an infrared imager as well as a laser spot tracker for use in laser-guided weapons delivery (Lantz, 2002, Touse, 2003). The quantum well was hence designed around the principal considerations of having the capability to detect wavelengths as low as $1\ \mu m$ for laser tracking as well as simultaneously detecting infrared radiation in the 8-12 μm window for infrared thermal imagery.

The overall detector performance is determined primarily by the characteristics of the long wavelength detector due to the use of doped quantum wells. The detailed study of the long wavelength response of the detector will provide information on the operating temperature and tunability of the detection wavelength in the 8-12 μm atmospheric window. These factors are important for deployment of detectors in military applications.

THIS PAGE INTENTIONALLY LEFT BLANK

II. QWIP BACKGROUND AND THEORY

A. SQUARE QUANTUM WELLS

The physics behind the operation of the quantum well photodetector is to a great extent similar to that of the extrinsic photoconductor. The QWIP detects infrared radiation by exciting bound electrons in a quantum well from their ground states to the excited states. These forms of transitions are called intersubband transitions as they occurred within the same band. The quantum wells have to be doped to populate the ground state. A typical square quantum well which is made from GaAs and AlGaAs is shown in Figure 7.

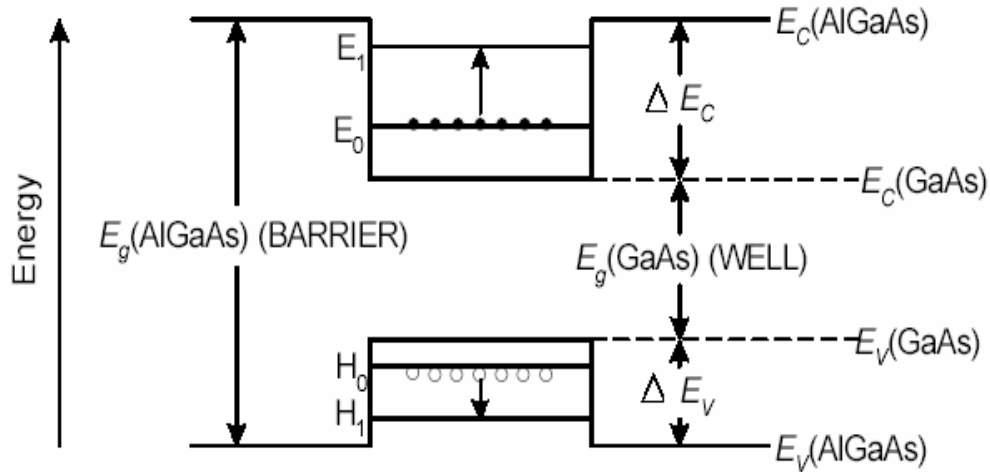


Figure 7. Square Quantum Well of AlGaAs and GaAs.
([From Hickey, 2002])

The energy levels within the well are created through the spatial localization introduced by the low band gap GaAs surrounded by the larger bandgap material AlGaAs. The quantum well is formed as a result of the difference in the energy bandgaps as depicted in Figure 7. In its simplest form, the energy levels can be derived from the Schrödinger equation for the infinite square well (Liboff, 2003). Note that for actual design of quantum well detectors

it is necessary to solve the finite quantum well problem instead of infinite well approximation.

$$-\frac{\hbar^2}{2m_e} \frac{\partial^2}{\partial z^2} \psi_n = E_n \psi_n \quad (2.1)$$

for which the wavefunctions and energy levels would be given respectively by: eq. (2.2) and eq. (2.3).

$$\psi_n(z) = \sqrt{\frac{2}{L}} \sin\left(\frac{\pi n z}{L}\right) \quad (2.2)$$

$$E_n = \left(\frac{\hbar^2 \pi^2}{2m_e L^2} \right) n^2 \quad (2.3)$$

where L is the width of the quantum well, m is the effective mass of electron in the well and n is an integer. The intersubband transition energy between the lowest and the first excited state can thus be calculated using eq. (2.4).

$$E_2 - E_1 = 3 \left(\frac{\hbar^2 \pi^2}{2m_e L^2} \right) \quad (2.4)$$

It can be easily deduced from the equation that the transition energy which is directly related to the wavelength of the absorbed radiation can be controlled by varying the width of the well. In this sense, customizing of the wavelength responses through bandgap engineering can be achieved by the choice of materials as well as their sizes. The other key factor here being that it is now possible to use semiconductor materials with larger bandgaps that are easier to

process and more stable, especially when there is a need to produce larger uniform detector arrays.

B. TYPES OF QWIPS

There are generally three distinct types of QWIPs that have been fabricated. They are the bound-to-bound, the bound-to-continuum and the bound-to-quasi-continuum QWIPs.

1. Bound-to-Bound QWIPs

In this case, both the ground and excited states are located within the quantum well. The infrared radiation absorption due to the intersubband transition from the ground state to the excited state has to be accompanied by the photoexcited carriers tunneling out of the well. These electrons would be transported by an external electric field in the continuum above the barriers thereby producing a photocurrent. This type of QWIPs has the narrowest absorption spectra albeit requiring a higher bias to ensure sufficient tunneling for the photoelectrons to be collected. A schematic diagram of operation of the detector is shown in Figure 8(a). Due to the high bias and tunneling requirement, the tunneling dominated dark current is relatively high. This category of QWIPs hence suffers from poor efficiency and detectivity as D^* is approximately inversely proportional to the square root of the dark current (Levine, 1993).

2. Bound-to-Continuum QWIPs

In order to enhance the transport properties of the photoexcited carriers and reduce the dark currents, the bound-to-continuum QWIPs, were later demonstrated to achieve better responsivity than the first type. By changing the width of the well, it can be seen that the excited state can be pushed into the conduction band above the barrier and the photocarriers need not tunnel through

any barriers before they are collected (Levine, 1993). However, due to the existence of the continuum of states above the barrier, it tends to produce a broader absorption peak. A schematic diagram of the operation of a bound-to-continuum QWIP is shown in Figure 8(b). The lower barrier height associated with these QWIPs can enhance thermionic emission which can impose a lower operating temperature.

3. Bound-to-Quasibound QWIPs

The third category which characteristically falls in between the first two, was the bound-to-quasibound QWIPs (Gunapala, 1997). As the name implies, these detectors have the excited state located exactly at the top of the barrier. The goal is to increase the barrier height to reduce the thermionic emission while efficiently collecting the photoexcited carriers. A schematic diagram representing this type of QWIP is shown in Figure 8(c).

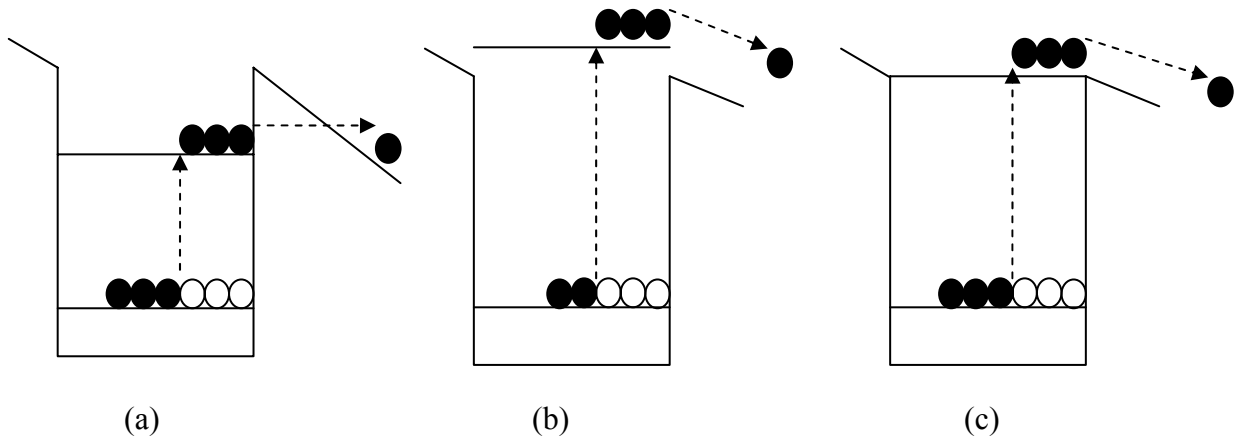


Figure 8. (a) Bound-to-Bound, (b) Bound-to-Continuum and, (c) Bound-to-quasibound QWIPs.

C. TRANSITION RATE AND OSCILLATOR STRENGTH

In the design of QWIPs, there are two key and related parameters that must be taken into consideration to ensure the functionality of the detector. These factors are fundamental to ensuring that transition of the electrons to the higher energy states occur and the resulting absorption is relatively strong. These are the transition selection rules and the oscillator strength. These quantities can be estimated using the Fermi's golden rule eq.(2.5) (Choi, 1997).

$$W = \frac{2\pi}{\hbar} \sum_{i,f} \left| \langle \Psi_f | V_p | \Psi_i \rangle \right|^2 \delta(E_f - E_i - \hbar\omega) \quad (2.5)$$

where W is the transition rate and the summation is carried out between the initial and final states that satisfy energy conservation in the δ function, and V_p is the interaction potential between the photon and electron (Karunasiri, 1984). The strength of the radiation absorption is ultimately determined by the transfer matrix element $\langle \Psi_f | V_p | \Psi_i \rangle$. This is usually evaluated using the dipole approximation for V_p and quantified by the oscillator strength given by eq.(2.6) (Mii, et al., 1990).

$$f = \frac{2m^*}{\hbar^2} (E_f - E_i) \langle z \rangle^2 \quad (2.6)$$

where the dipole matrix element $\langle z \rangle$ is given by eq.(2.7)

$$\langle z \rangle = \int \phi_f(z) z \phi_i(z) dz \quad (2.7)$$

For a symmetric potential well, it can be deduced from eq. (2.7) that the integral will yield a finite value if ϕ_f and ϕ_i have opposite symmetry, and will yield

zero when they are of the same symmetry. In the case of a square quantum well, since ϕ_2 and ϕ_1 have opposite symmetry, the integral will yield a finite result. However, ϕ_3 and ϕ_1 would have the same symmetry causing the value of the integral to go to zero. The consequence of this is that for a square quantum well, transition will only occur for states with a difference in quantum numbers that is odd (i.e. 1 to 2, 1 to 4, etc). This can present serious problems to achieve certain desired transitions. A convenient and solution to this problem is to break the symmetry of the well, for example, by using an asymmetric step quantum well.

According to the oscillator strength given in eq. (2.6), it can be further deduced that for quantum wells grown along the z-direction, the photon electric field must also have a component parallel to the z direction in order to induce the transition (Levine, 1993). This means that the normal incidence of radiation (i.e., along z-direction) will not result in any absorption. This is known as the polarization selection rule. A common approach to overcome this problem is to polish the substrate of the detector to a 45° angle edge facet in a waveguide geometry to facilitate IR coupling as shown in Figure 9. In this way, the transverse E field will carry a component in the z direction to enable the transition to take place.

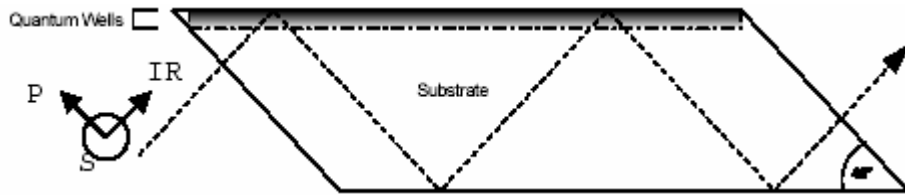


Figure 9. 45° Facet Geometry to Overcome Polarization Selection Rule.
([From Touse, 2003]).

An alternative solution is to mount the device such that the infrared beam incident the surface at the Brewster angle (Levine, 1993), which is 73° for the

case of GaAs, to produce a component of the optical electric field along the growth. For fabrication of 2-D focal plane arrays, the use of diffraction grating to couple IR radiation into the devices is usually employed as shown in Figure 10.

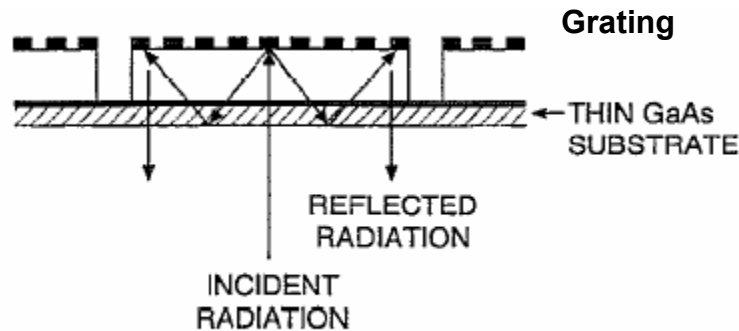


Figure 10. Diffraction Grating for Coupling of IR Radiation.
([From Levine, 1993, pp R65]).

D. TUNING OF WAVELENGTH USING STARK EFFECT

In addition to enabling transitions between states that were previously not possible due to symmetry, the asymmetric quantum wells have another important feature. When a bias is applied across the quantum well to create the electric field to facilitate the collection of the excited electrons, the shape of the quantum well deforms and the transition energies change accordingly. This change in the transition energy is relatively small in the case of a square well and is substantial in an asymmetric step quantum well. The consequence of this is the quantum confined stark effect, which is commonly referred to the shift of the transition energy in a quantum well as a function of the applied electric field (Yuh, et al, 1989). In addition, the transition energy shift in square quantum wells is towards higher energy while in the case of the step quantum well, the peak can be either Blue shifted (shorter wavelength) or Red shifted (longer wavelength) (Mii, et al, 1990).

The Stark effect in a step quantum well can be explained further with the help of Figure 11, where the ground state E_1 is confined by the small quantum well and second and third states, E_2 and E_3 , are bounded by the large well, which under an external bias follow the centroid of the large well. Within the first order of approximation, the bound state energy of a quantum well with respect to the well centroid is independent of the applied electric field as long as the potential drop across the well is smaller than the bound state energy (Mii, et al, 1990). This means that the ground state, E_1 , will track the centroid of the small well, while the second and third state, E_2 and E_3 , will track the centroid of the larger well. Due to the asymmetric nature of the step well structure and depending on the direction of the applied field, the sub-level energies can move closer or further resulting in either Red (increase in wavelength) or Blue (decrease in wavelength) shift respectively (Yuh, et al, 1989). This is markedly different from the case of the square well where because of its symmetry the shifts are the same for all the states and there is no first order energy shift. In this case the observed shift is due to second order effects (Harwit, et al, 1987). The difference in potential energy drops between the centroids of the small and large well produces a “first-order” Stark effect and the transition energy shifts are approximately equal to this difference. In a square well, because of the absence of first order Stark effect, the shift is an order of magnitude smaller than in step quantum wells (Karunasiri, 1990). To achieve a large energy shift in a square well, a strong field is needed which deforms the well into a triangular well. Under high bias the electrons in the well can be field ionized which increases the leakage current. Effectively, the step quantum well is equivalent to a square well under extremely high fields, but without the negative effect of the excessive leakage current present (Mii, et al, 1990).

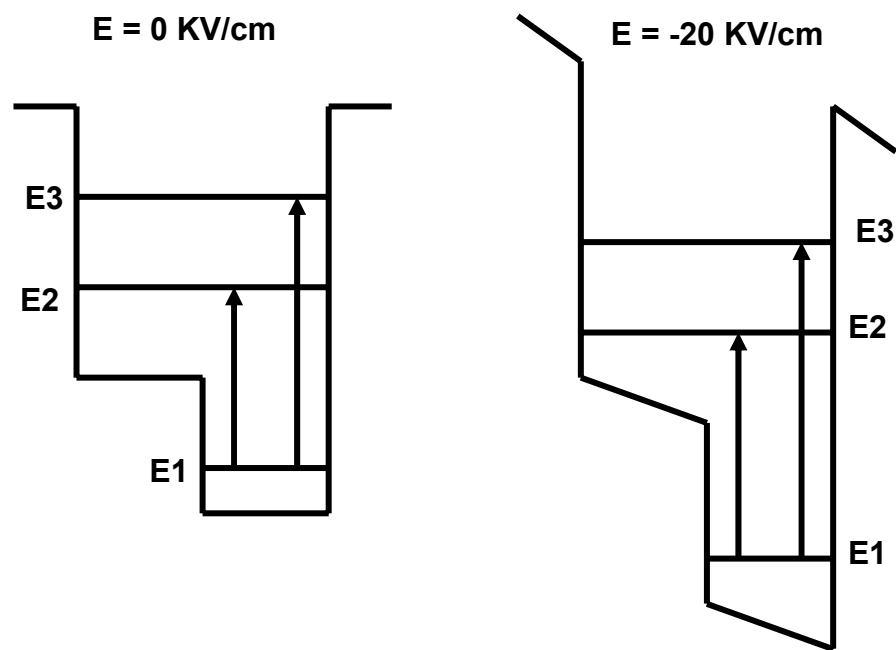


Figure 11. Linear Stark Effect in a Step Quantum Well.

THIS PAGE INTENTIONALLY LEFT BLANK

III. STEP QUANTUM WELL STRUCTURE

A. SELECTION OF MATERIALS FOR QWIP

As discussed in Chapter II, in order to form the step quantum wells, there is a need to combine materials of different bandgaps to engineer the desired transition energy to produce wavelength response in the 10 μm range. For such design purposes the relationship between bandgap and lattice constant of semiconductors used is important (see Figure 12). Besides relying on the bandgap information to choose the desired materials, it is also important to ensure that the lattice constants are matched to minimize the generation of misfit dislocations. The combination of the different materials in the structure will cause their bandgap energies and effective masses to change in accordance with the Vegard's Law with a bowing parameter to account for the non-uniformities of alloying as given by eq. (2.8) and eq. (2.9) (Singh, 1993).

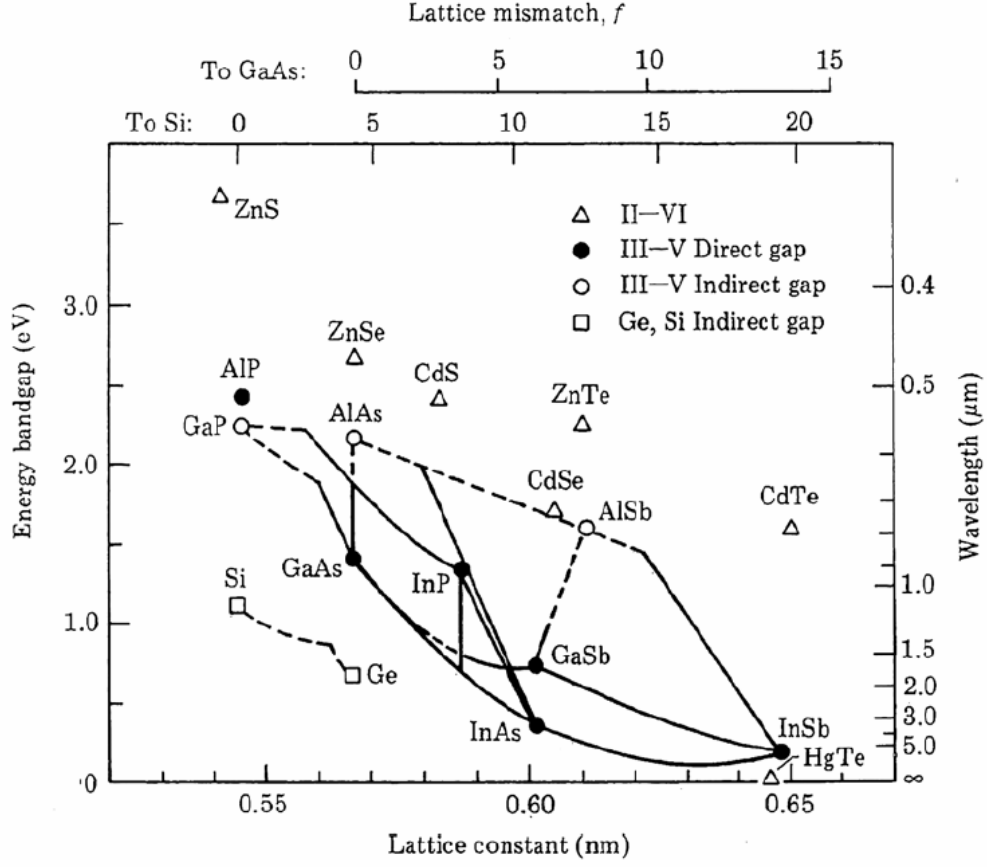


Figure 12. Diagram of Bandgap vs Lattice Constant for Different Materials
([From Tu, 1992, pp 158]).

$$E_g^{A_xB_{1-x}} = xE_g^A + (1-x)E_g^B + x(1-x)C_{AB} \quad (2.8)$$

$$\frac{1}{m_{A_xB_{1-x}}^*} = \left(\frac{x}{m_A^*} + \frac{1-x}{m_B^*} \right) \quad (2.9)$$

where x is the molar percentage of material A and C_{AB} is the experimentally determined bowing parameter.

The design of step quantum well structure used in this study was carried out using ternary alloy of InAs and GaAs. Besides being able to meet the desired wavelength response, a key factor in choosing these materials was the mature

technology available in growing them. However, it can be seen from Figure 12, that there was still the need to be cautious in limiting the amount of In to be used in order to reduce the lattice mismatch due to difference in lattice constants of GaAs and InAs. The molar percentages of In used were 0.1 for the step and 0.3 for the well.

B. FABRICATED STEP QWIP TEST DETECTOR

In order to enhance the probability of photon capture, multiple quantum well structure were employed instead of just one step well by having large bandgap GaAs barriers between the quantum wells to prevent tunneling through to the adjacent wells (Levine, 1993). The final fabricated test detector consisted of 25 step quantum wells with 4 nm wide well and 4 nm wide step. A 30 nm GaAs barrier between wells was used to reduce the undesired tunneling of electrons between wells. The QWIP was grown by Molecular Beam Epitaxy (MBE) as it was the preferred process that is capable of producing high-quality layers with good precision in thickness, doping, and composition. A drawing of the QWIP structure is shown in Figure 13 and Table 2 details the wafer specifications.

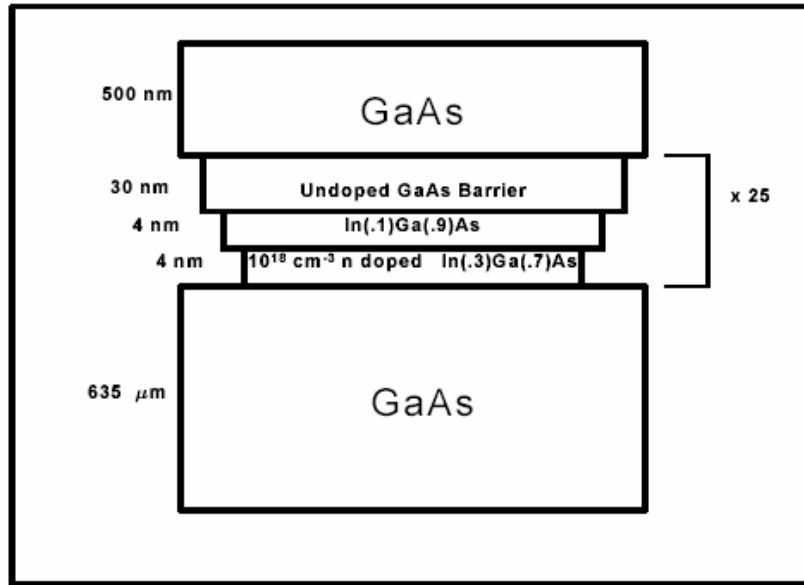


Figure 13. Schematic Diagram for Structure of Fabricated Test Detector.
([From Touse, 2002, pp 19]).

Substance	Mole %	Thickness (A)	Si Doping Concentration (cm ⁻³)
GaAs		5000	1E+18
GaAs		300	
InGaAs	10	40	
InGaAs	30	40	1E+18
GaAs		500	
GaAs		8000	1E+18
GaAs		6.35E+06	

Table 2. Details of Wafer Specifications.
([From Touse, 2002, pp 19]).

The band diagram of the step quantum well shown in Figure 13 is depicted in Figure 14. There are two energy levels in the conduction band, one in the narrow well while the other in the wide well near the top of the barrier. The latter has been deliberately engineered so that the photoexcited electrons do not need to tunnel through the barrier to be transported and collected, making this a bound-to-continuum QWIP. The asymmetric nature of the step quantum well

enables the tuning of detection wavelength.

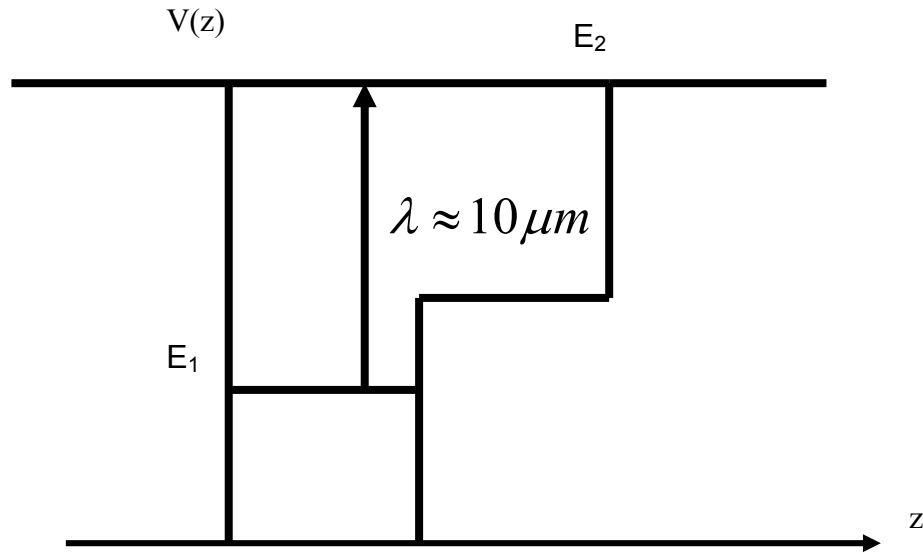


Figure 14. Asymmetric Step QWIP Structure with Energy Levels.

C. ABSORPTION USING 45° FACET WAVEGUIDE

As mentioned in Chapter II, to ensure absorption of IR light, the polarization selection rule has to be satisfied. This was achieved by polishing the edges of the sample to an angle of 45° to allow for internal reflection and absorption as the light passes through the quantum wells. The completed waveguide along with the sample is shown in Figure 15. IR radiation entering normally on the edge will have component in the growth z -direction of the well, this resolved component of the electric field would have to be factored in the subsequent calculation of the responsivity in Chapter IV.

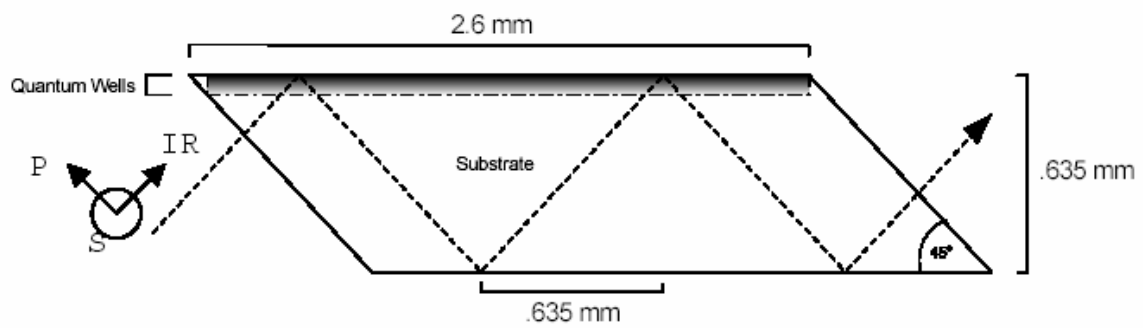


Figure 15. Dimensions of 45° Angled Facet Geometry Waveguide.
 ([From Touse, 2002, pp 26])

IV. EXPERIMENTAL SETUP AND RESULTS ANALYSIS

A. PHOTODETECTOR CHARACTERIZATION SYSTEM

The key equipment used for this thesis was the computer controlled photodetector characterization system that was assembled in an earlier thesis (Herdlick, 2002), to measure the responsivity of the test detector under different conditions of bias and temperature. Pictures of the equipment setup, which can be divided to 3 modules, are shown in Figures 16, 17 and 18.

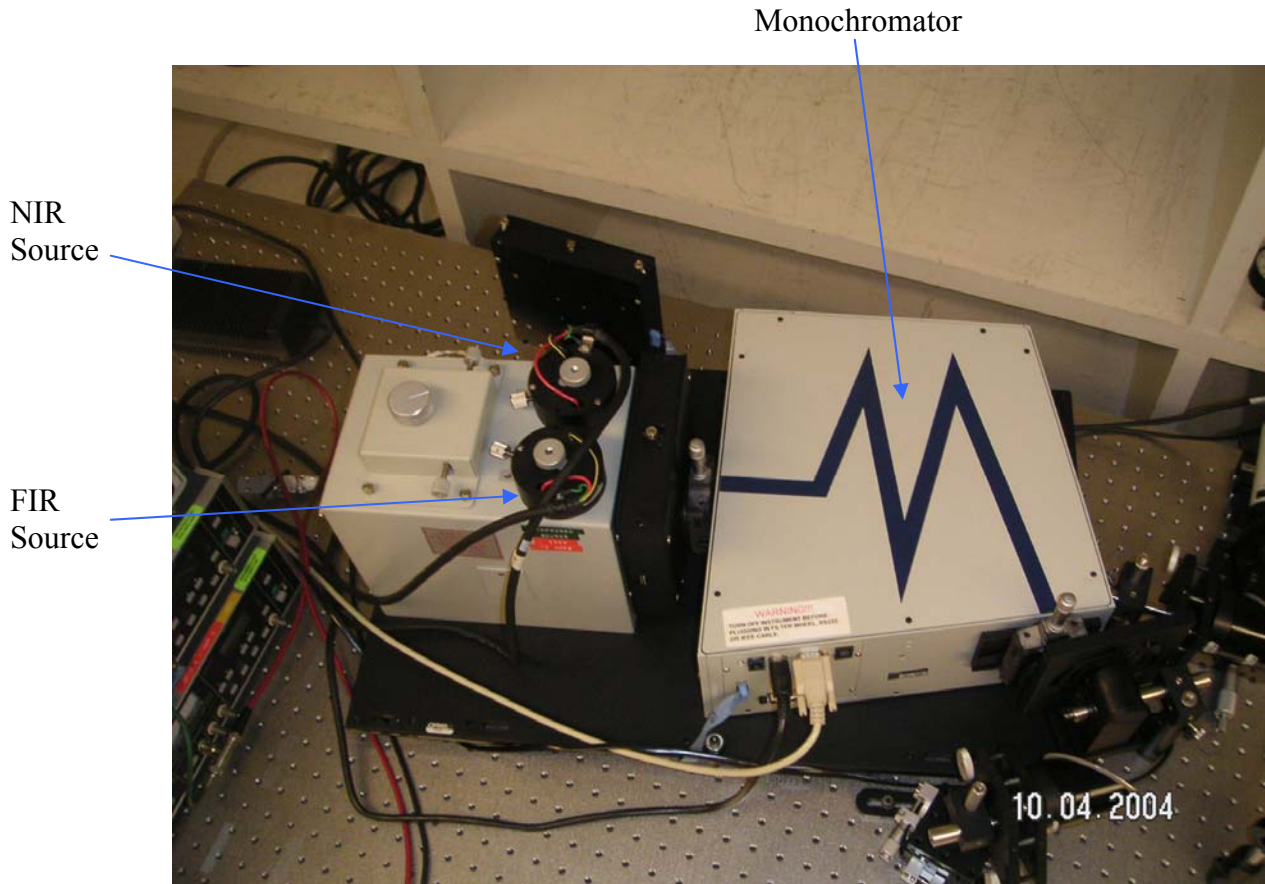


Figure 16. Characterization System Module 1: IR Sources and Monochromator.

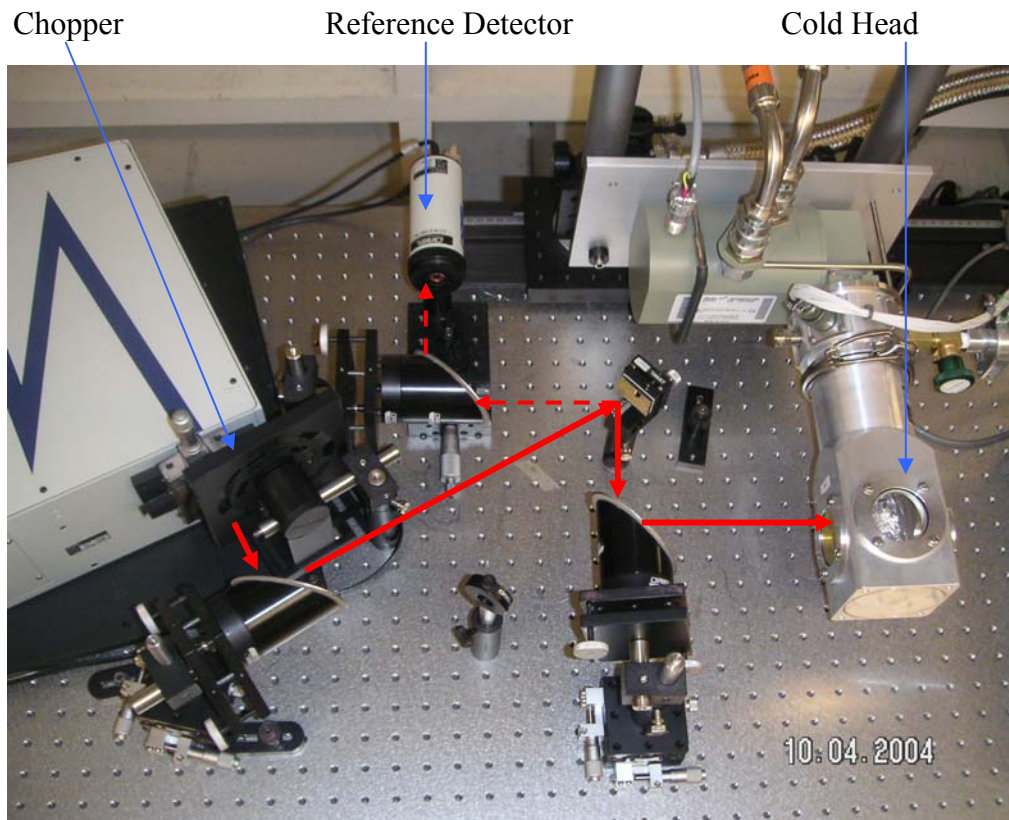


Figure 17. Characterization System Module 2: Mirror Configurations Directing IR Rays to Test and Reference Detectors.

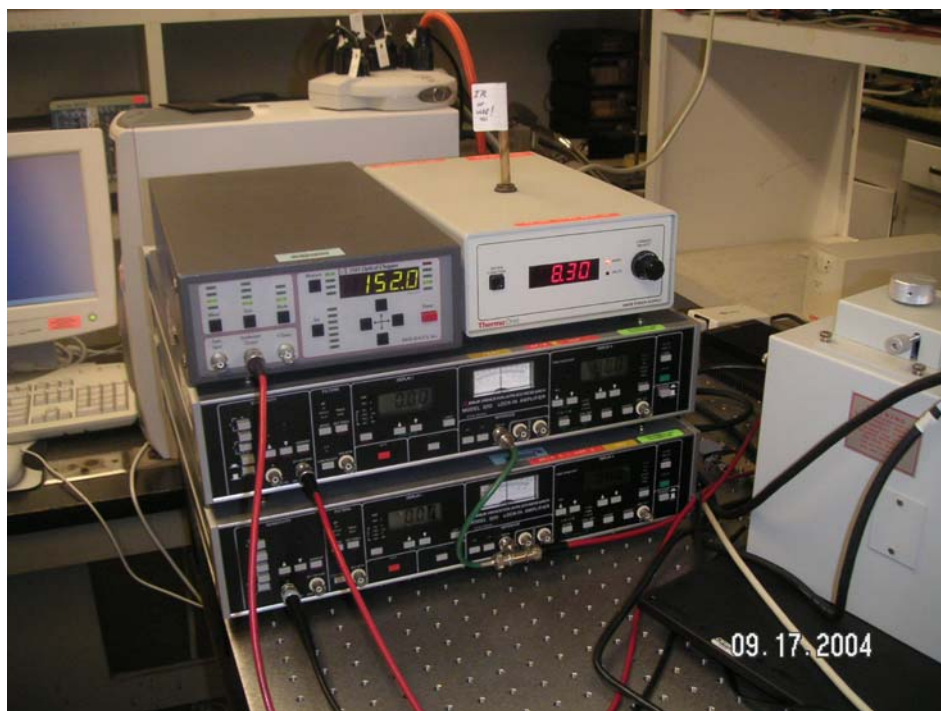


Figure 18. Characterization System Module 3: Chopper Control and Lock-in Amplifiers for Monitoring Test and Reference Detector Outputs.

The setup was divided into three modules. Firstly the generation and control of energy module (Figure 16) provides the required sources of radiation at the desired wavelengths of interest. Two types of sources covering the NIR and FIR windows were selectable for transmission into a monochromator. The radiation sources were the Oriel 6333 Quartz-Tungsten-Halogen (QTH) Lamp and the Oriel 6363 IR element, respectively. Due to the non-uniformity of power incident on the test detector at different wavelengths, a reference detector with known responsivity was employed for normalization purposes. Selectable filters were also used for the elimination of second order diffracted beams from the gratings.

The second module consisted of the beam control module (Figure 17), which was a collection of all the required mirrors to reflect the radiation on to the test detector as well as the reference detector. The mirror with the golden surface in the center can be rotated to reflect radiation either to the test detector or the reference detector for measurement. Prior to using the fixed mirror, an attempt was made to fabricate a rotating platform with five of the same mirrors so that the radiation can be reflected and measured concurrently for both detectors hence eliminating the need for manual rotation. The same chopper motor was used to power the rotating platform for the mirrors so as to facilitate the use of the same set of chopper for the lock in amplifiers. Although, it worked well with the NIR, the signal was too weak in the FIR due to the reduced duty cycle of energy falling on the detectors. A picture of the rotating mirror is attached in Appendix A. Also part of the second module was the cold head which housed the detector. The cold head was effectively a refrigerator employing cryogenic closed loop refrigeration to cool the detector down to the required temperatures for measurement.

The last module was the detection and measurement module (Figure 18), which basically consisted of lock-in amplifiers coupled to an optical chopper control. The optical chopper modulated the signal to be detected by the amplifiers and in the process limiting the bandwidth to 1 Hz around the chopping

frequency. The lock-in amplifiers were synced to the chopping frequency and the readings were directly fed to the computer for display as well as data storage for subsequent analysis.

The instrumentation in the entire setup and the running of the experiments were controlled using the LABVIEW program written for the photodetector characterization system.

B. DEVICE PIN DIAGRAM

For studying and analyzing the performance of the step quantum well detector, a piece of the sample containing eight mesa diodes was mounted on a ceramic package with electrical leads. The gold wirebonding was used to connect the devices with the electrical leads. Six of the devices were located on the outside of the package facing the light input, while two devices were situated on the inside as shown in Figure 19.

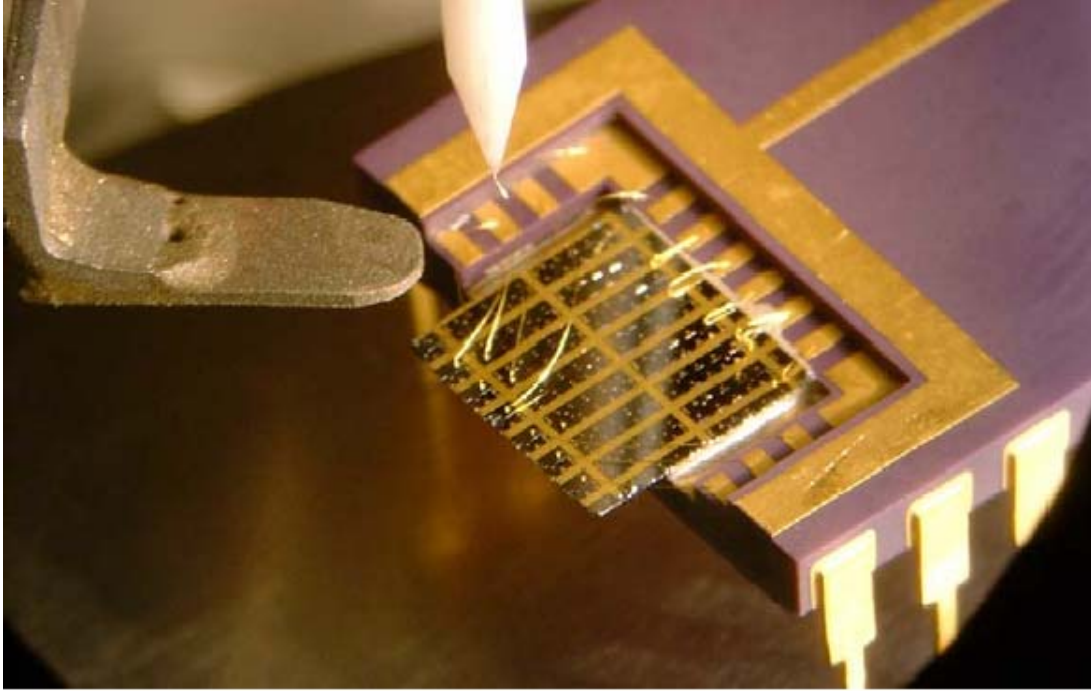


Figure 19. Picture of Test Detector Showing Wire Bonding.
([From Touse, 2002, pp 34]).

In order to ensure accurate and consistent measurements of the correct devices, a schematic diagram of the wiring of the devices to the package and the groundings was drawn as shown in Figure 20. The pads on the package were connected to the top of mesa of different devices and the ground to the bottom contact layer. The devices were labeled C, D, E, F, G, H, J, L, while GD represents ground. The devices facing the incident infrared beam have surface area of $0.3 \times 0.3 \text{ mm}^2$ square active areas. The wirings from the package were carefully fed to a junction box which housed a breadboard, so that subsequent measurements can be made. A picture of the junction box has been attached in Appendix A.

For the purpose of this thesis, device D was selected as the device under test. To ensure that the device was working properly, resistance checks were constantly done at room temperature and the various temperatures that the devices were cooled to. The room temperature resistance of the devices was about 11Ω , while at the other temperatures, the resistances were checked

against the other devices to ensure the values increase as temperature is reduced.

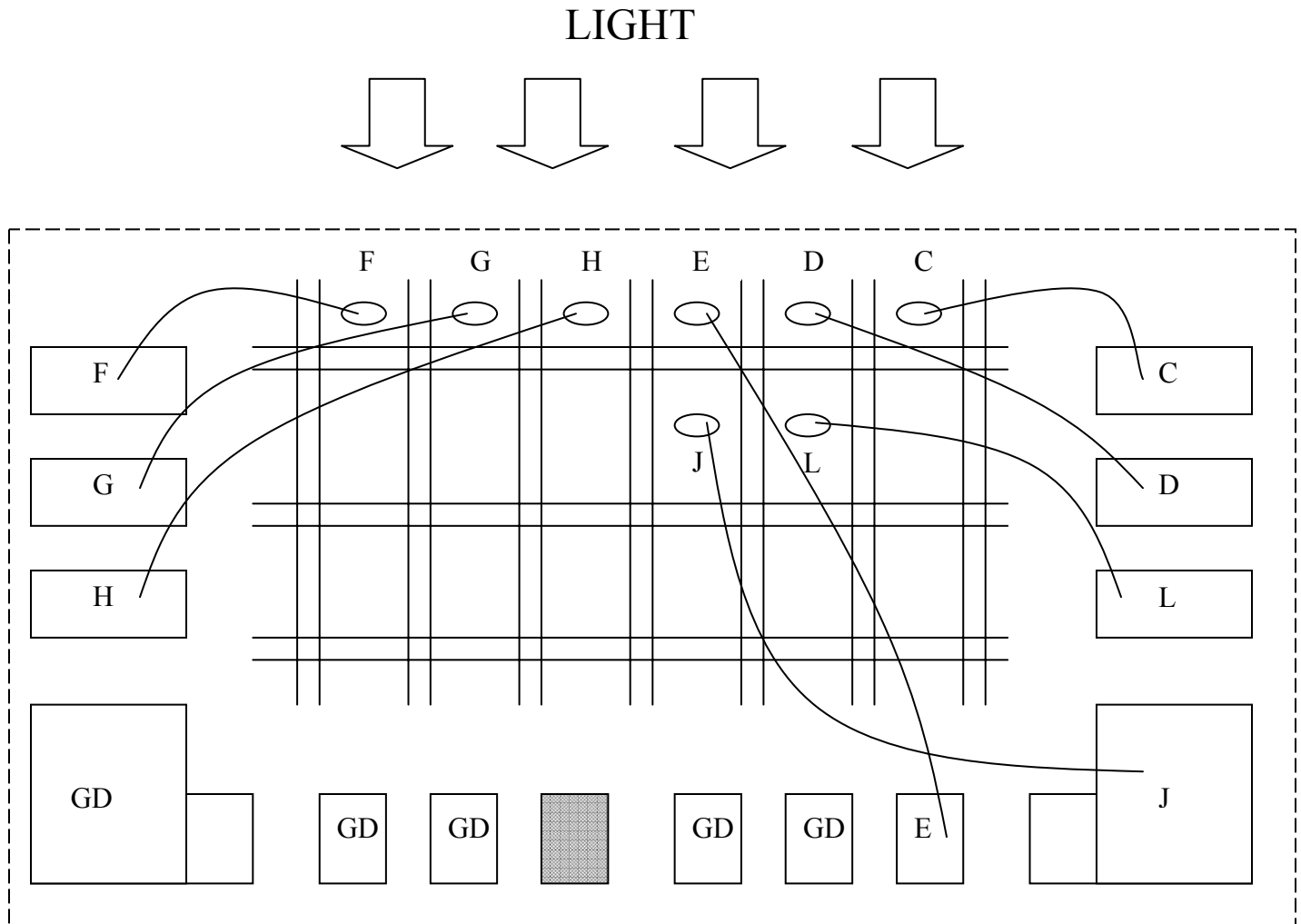


Figure 20. Schematic Diagram of the Test Detectors Wired to the Package for Manipulations and Measurements.

B. CALCULATION OF RESPONSIVITY

To estimate the responsivity, the photocurrents generated by the test detector as a result of the absorption of the radiation have to be measured. The responsivity of the reference detector, as obtained from the supplier's specification sheet, was about 1000 V/W for the wavelength range of interest. The specification sheet for the reference detector can be found in Appendix B. With the equipment setup for the same amount of intensity to be intercepted by both the test detector (ϕ_{det}) and the reference detector(ϕ_{ref}), the power per unit area intercepted by the test detector can be calculated based on the voltage generated by the reference detector divided by its known responsivity, and dividing over the reference detector's surface area (A_{ref}) as shown in eq. (4.1).

$$\phi_{det} = \phi_{ref} = \frac{P_{ref}}{A_{ref}} = \frac{V_{ref}}{R_{ref} A_{ref}} \quad (4.1)$$

where V_{ref} is the voltage generated by the reference detector, P_{ref} is the power on the reference detector and R_{ref} is the known responsivity of the reference detector. The reference detector used has a diameter (d) of 5 mm. Depending on the slit width (S_w) of the monochromator used (2 mm), the surface area radiated on the reference detector can be calculated as $A_{ref} = d \times S_w$. The power detected by the test detector (P_{det}) could then be simply calculated by multiplying the intensity on the test detector, which in this case would be the same as that on the reference detector, with the test detector's surface area which was $0.3 \times 0.3 \text{ mm}^2$ for the devices on the outer surface of the package in the direct path of the light.

$$P_{det} = \phi_{ref} \times A_{det} = \frac{P_{ref} \times A_{det}}{d \times S_w} = \frac{V_{ref} \times A_{det}}{R_{ref} \times d \times S_w} \quad (4.2)$$

Since it was the photocurrent that was being collected, the responsivity would be defined in terms of current per watt as in eq. (4.3).

$$R_{\text{det}} = \frac{I_{\text{det}}}{P_{\text{det}}} = \frac{I_{\text{det}} \times R_{\text{ref}} \times d \times Sw}{V_{\text{ref}} \times A_{\text{det}}} \quad (4.3)$$

However, there were also other factors that needed to be considered to arrive at the final responsivity of the detector. These included the transmittance of the GaAs substrate and the zinc selenide window of the cold head where the detector is situated for measurement at low temperature, as well as the geometrical factor since the light was not incident normally on the detector. As the radiation had to pass through the GaAs substrate, the transmission coefficient of the latter needed to be factored in the responsivity calculation. This could be obtained from the refractive indices n_1 and n_2 through eq. (4.4) for the Air-GaAs interface.

$$T_{GaAs} = 1 - \frac{(n_1 - n_2)^2}{(n_1 + n_2)^2} = 0.68 \quad (4.4)$$

Since the light was incident onto the window of the chamber of the cold head housing the test detector, the power also needed to be corrected to account for the reflectivity or the transmission coefficient of zinc selenide window, which has transmission coefficients ranging from 0.65 to 0.73 depending on the wavelengths of interest based on the supplier's specification sheet. The transmission of ZnSe as a function of wavelength can be found in Appendix B. Finally, account has to be taken also for the fact that the light was incident normal on the 45° facet, which translated to reduction of detector area by a factor

of $1/\sqrt{2}$. Hence, the resultant formula for the responsivity is given by eq. (4.5).

$$R_{\text{det}} = \frac{I_{\text{det}}}{P_{\text{det}}} = \frac{I_{\text{det}} \times R_{\text{ref}} \times d \times Sw \times \sqrt{2}}{V_{\text{ref}} \times A_{\text{det}} \times T_{\text{ZnSe}} \times T_{\text{GaAs}}} \quad (4.5)$$

C. MEASUREMENT OF RESPONSIVITY

One of the distinguishing characteristics of QWIPs is that in order to operate effectively, they need to be cooled to a sufficiently low temperature to reduce the effects of thermionic emission or dark current. As such, the test detector was cooled to a temperature of 10 K for the measurement of its responsivity under different bias. In addition, the performance of the test detector under different temperatures was also studied by keeping the bias fixed and increasing the temperature from 10K to 50K. The results will be presented and discussed in the next few sections.

1. Bias Dependence of Responsivity

With the temperature fixed at 10K, the photocurrents for the test detector under different bias were measured, and the responsivities calculated using eq. (4.5). In the setup of the measurement, positive bias refers to the application of a positive voltage on the top of the mesa relative to the bottom electrode. Figure 21 shows plots of the resultant responsivity as a function of wavelength for a set of bias voltages.

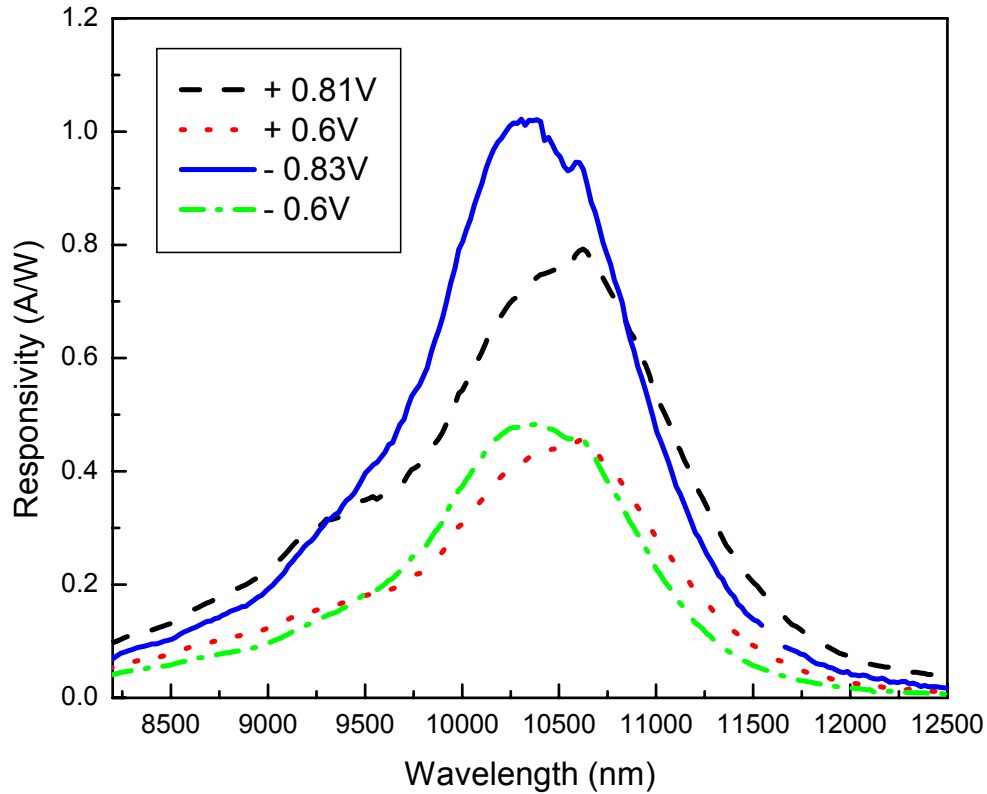


Figure 21. Responsivity as a function of wavelength at $T = 10$ K for a set of bias voltages.

It can be observed from the plots that the responsivity increased with increasing magnitude of the bias in either direction. This was expected because the larger bias resulted in a stronger electric field across the quantum wells that increases the drift velocity of electrons, thereby producing a larger photocurrent. This effect was apparent until saturation began to occur at just under 1 V when the large electric field resulted in higher leakage current due to tunneling which causes the detector to breakdown.

From the plots above, it was also apparent that for similar voltages, the negative biases recorded higher responsivities as compared to the positive biases. This could be explained with the help of Figure 22 (a) and Figure 22 (b), which detailed the energy states along with the well structure under opposite bias conditions, and how electrons that transit to the excited state would be

transported out to be collected as photocurrent. In the design of the detector, the transition of energy states to generate the response in the FIR involved a transition from the ground state in the small well to the continuum states which resided above the large well. When the quantum well was under a negative bias, the structure of the conduction band will be bended in a manner depicted in Figure 22 (a). As the excited state tracked the large well and the ground state tracked the small well, the excited state E2 move upwards further in to the continuum which resulted in an increase in the transition energies or a blue shift in the peak wavelength response. It can be seen from the figure that with the new E2 state further up in the continuum, it became easier for the electrons to be transported, thereby producing a larger photocurrent or responsivity. The blue-shifts for positive bias conditions were clearly observed in Figure 21.

On the other hand, when a positive bias was applied to the quantum well, the electric field would cause conduction band to be bended in a manner depicted in Figure 22(b). Similarly, when the two states tracked the centroids of their respective wells, the excited state E2 would be moved deeper in to the well which would cause a decrease in the transition energy or a red-shift in the peak wavelength response. It can be seen then that with the new E2 state within the well, the electrons that transited in to the excited state would then have to tunnel through or overcome the slight barrier before they could be collected as photocurrent. The increased difficulty resulted in a decrease in the photocurrent and hence responsivity. Similarly, the red-shift for positive bias were clearly observed in Figure 21.

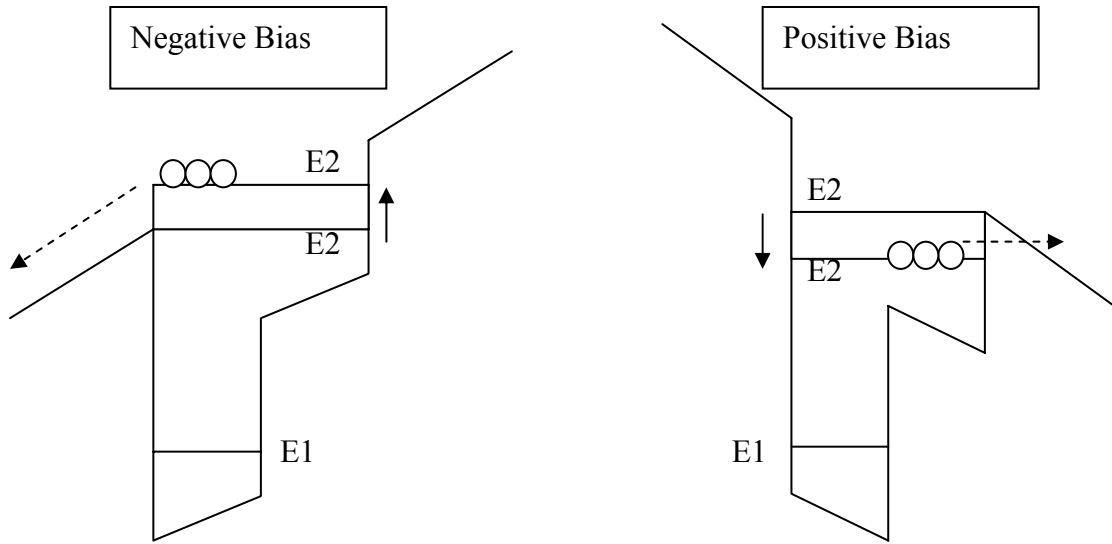


Figure 22. Conduction Band Structure and Electrons Transport (a) Under Negative Bias and (b) Under Positive Bias.

Due to the resonance nature of the intersubband transitions, the QWIP would detect a narrow band of wavelengths centered on the energy separation between ground and excited state. This was evident from the plots of the responsivities, although in this case, due to the bound-to-continuum nature of the QWIP, there was a broadening that could be attributed to the availability of additional energy states in the continuum. The maximum peak responsivity for the test detector under a negative bias of 0.83 V was found to be 1.022 A/W occurring at a peak wavelength of 10.32 μm . The measured responsivity was relatively higher than most of the measured responsivities that have been reported for similar structures (Martinet, et al, 1992, Ting, et al, 1997).

2. Stark Effect

As mentioned earlier, it was evident that as the bias voltage across the

device was varied, the peaks of the responsivity plots were shifted and the shifts became more pronounced with increasing bias voltage. The shift in the peak wavelength was due the asymmetric nature of the step quantum well as explained in Chapter II. To see the effect more clearly, the plots for the normalized responsivities for the test detector under +0.81 V and -0.83 V biases are reproduced in Figure 23.

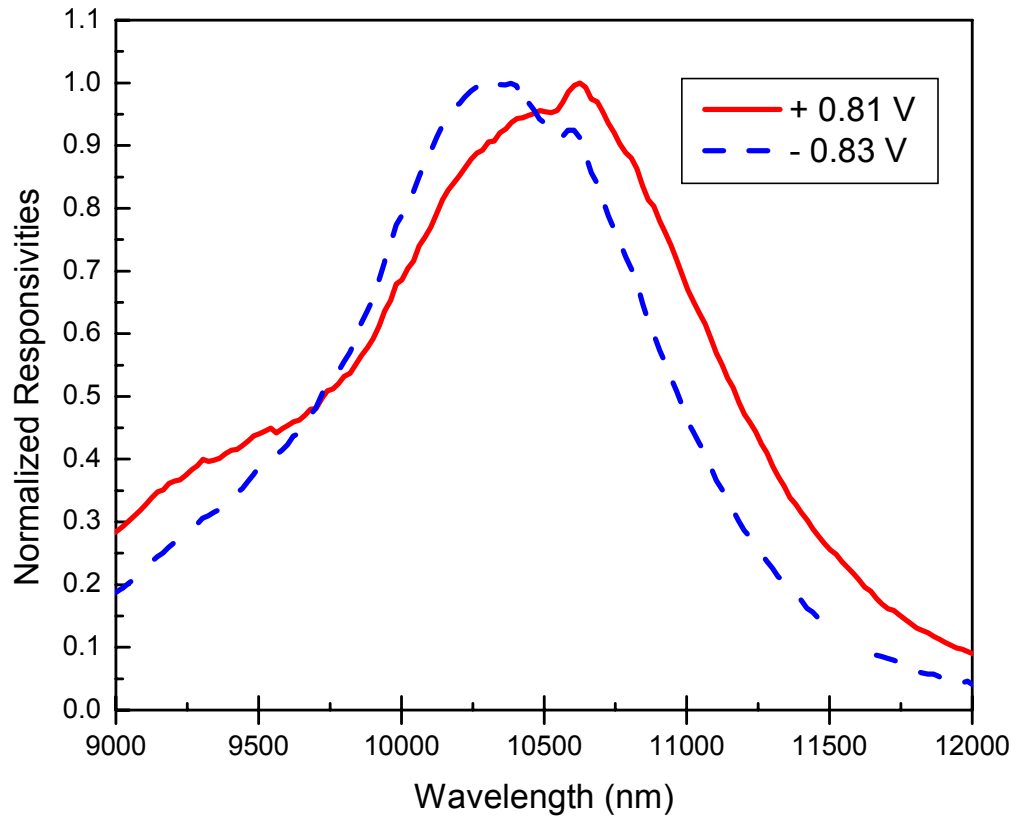


Figure 23. Normalized Responsivities Showing Stark Effect.

It could be observed that as the bias voltage was varied from -0.83 V to +0.81 V, the peak wavelengths of the responsivity curves were red-shifted from 10.31 μm to 10.62 μm respectively. In energy terms, there was an equivalent shift (ΔE_{shift}) of 3.6 meV.

With an effective change in the bias of 1.64 V, the applied field across the 25 quantum wells was calculated to be 17.26 KV/cm. Therefore, the measured Stark shift in response to the electric field was 0.21 meV/KVcm⁻¹. The magnitude of Stark effect measured provided an indication of the tunability of the test detector under bias conditions. For example, by changing the bias applied on the test detector, the desired response peak of the test detector could then be modified accordingly.

Theoretically, the shift in energy could be approximated by eq. (4.6) (Mii, et al, 1990), where e is the electron charge, F is the electric field and b is the distance between the center of small well and the center of the large well. From Table 2, since the small well was 4 nm wide while the large well was 8 nm wide, b was 2 nm in this case.

$$\Delta E_{shift} = eFb \quad (4.6)$$

The theoretical energy shift was calculated to be 3.45 meV which agrees well with the measured energy shift of 3.6 meV.

To verify that the Stark shifts did obey a linear relationship given by eq. (4.6), the Stark shifts for the other bias voltages were calculated and tabularized in Table 3. The measured energy shifts against the electric field were plotted in Fig 24. The predicted linear Stark shift using eq. 4.11 was also plotted for comparison.

Bias Voltage (V)	Peak Wavelength (nm)	Energy (meV)	Energy Shift (meV)	E field (KV/cm)	Energy Shift / E Field (meV/KV cm ⁻¹)
-0.83	10310	120.6	-	-	-
-0.60	10350	120.0	0.6	2.42	0.25
-0.40	10390	119.6	1.0	4.53	0.22
-0.15	10450	119.0	1.6	7.16	0.22
+0.15	10530	118.1	2.5	10.32	0.24
+0.60	10600	117.3	3.3	15.05	0.22
+0.81	10620	117.0	3.6	17.26	0.21

Table 3. Measured Energy Shifts due to Stark Effect for Different Electric Fields.

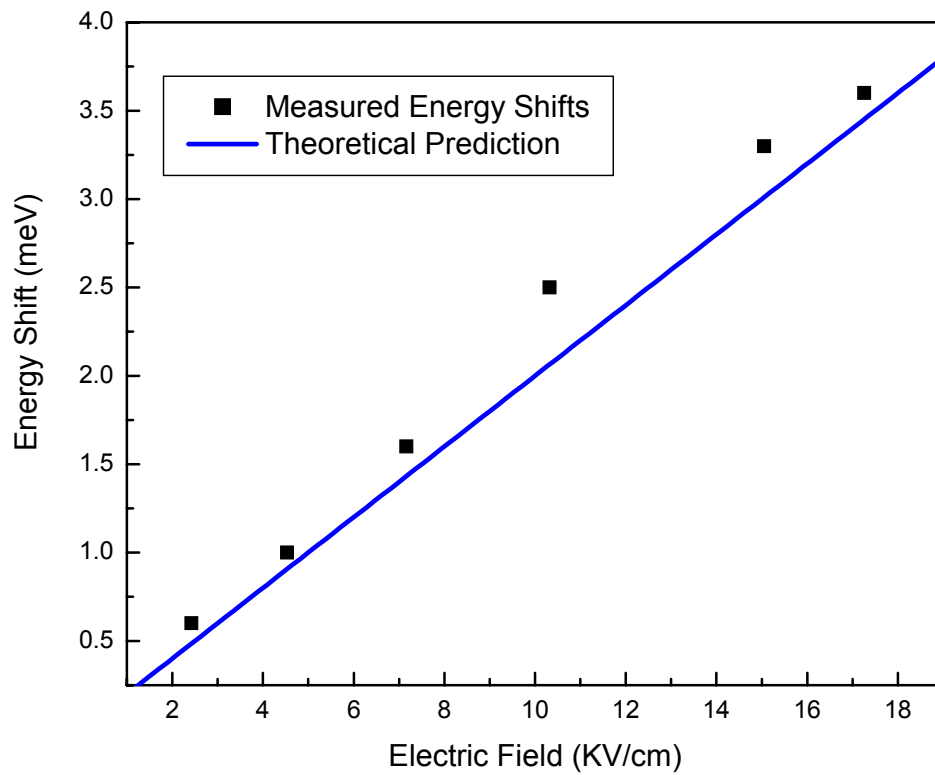


Figure 24. Plots of Measured and Predicted Stark Shifts vs Electric Field.

3. Temperature Dependence of Responsivity

To further establish the performance of the test detector, the responsivity of the device was measured for different temperatures while keeping the bias voltage fixed at 0.15 V. The responsivities for the test detector under both positive and negative bias conditions were measured for temperatures ranging from 10 K to 50 K and plotted in Figure 25 and Figure 26.

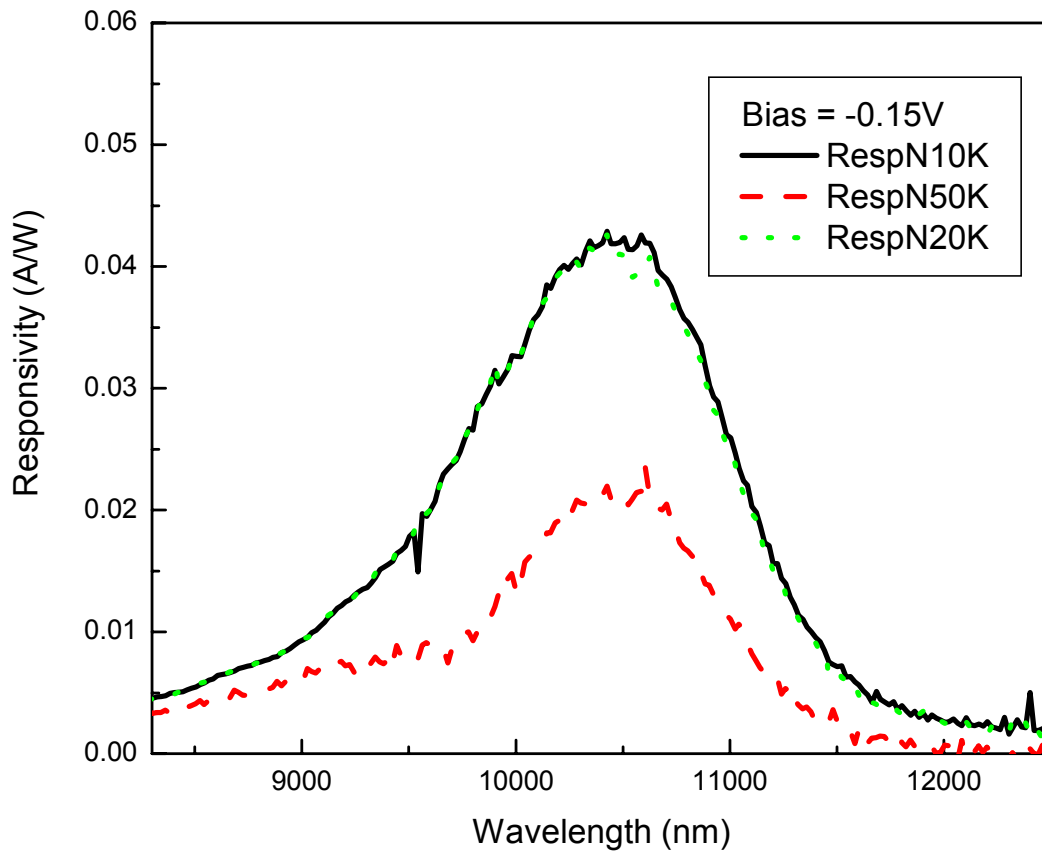


Figure 25. Responsivity at -0.15V Voltage Across the Detector for Different Temperatures.

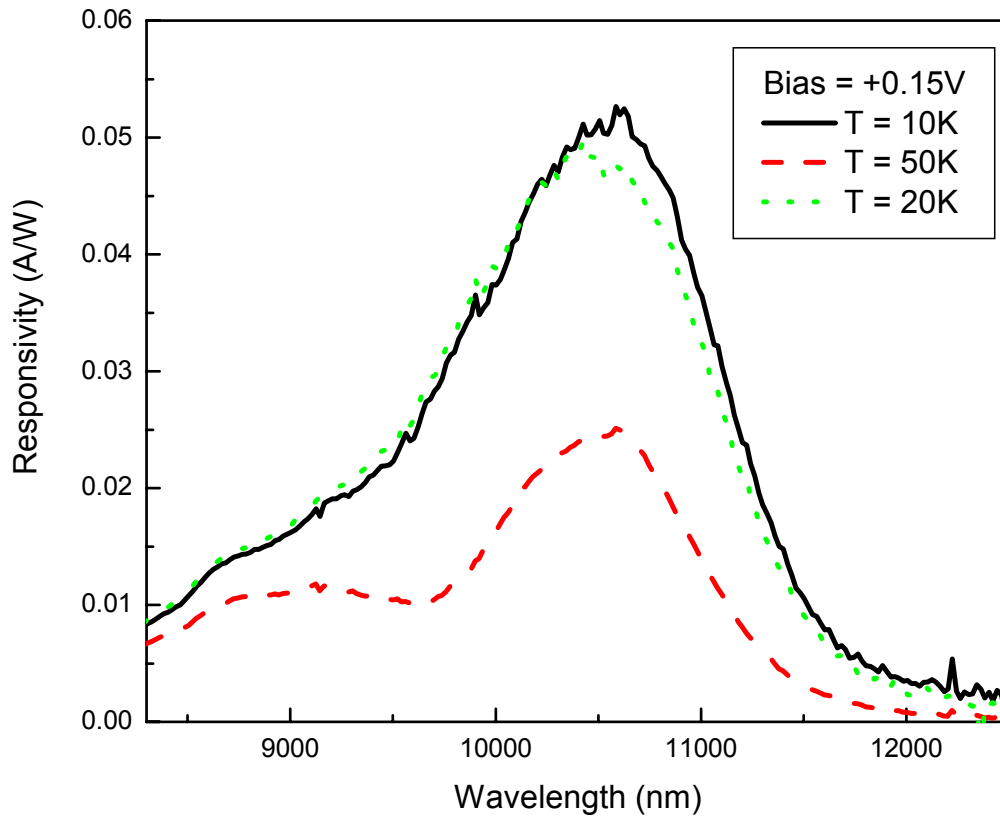


Figure 26. Responsivity at +0.15V Voltage Across the Detector for Different Temperatures.

It was apparent from the plots that at higher temperatures the responsivity of the test detector decreased. This was expected as at higher temperatures, the drift velocity of the electrons will decrease as a result of the presence of more phonons. This will in turn result in a smaller current causing the responsivity to also decrease.

5. IV Characteristics and Dark Current Measurement

Besides measuring the responsivities of the detector, the IV characteristics of the test detector were also measured using an Agilent 4155B semiconductor parameter analyzer. The I-V characteristics can serve many useful purposes, including being used to determine the amount of leakage current or dark current, the suitable operating range of voltages, and barrier height of the quantum well. In addition, the Background Limited Performance of the device can be extracted using dark currents at various temperatures.

First, the I-V characteristics of the test detector exposed to the background infrared radiation were measured for a set of different temperatures. They were plotted and shown in Figure 27. The currents recorded in these curves included both the dark currents and the photocurrent generated by the background infrared radiation.

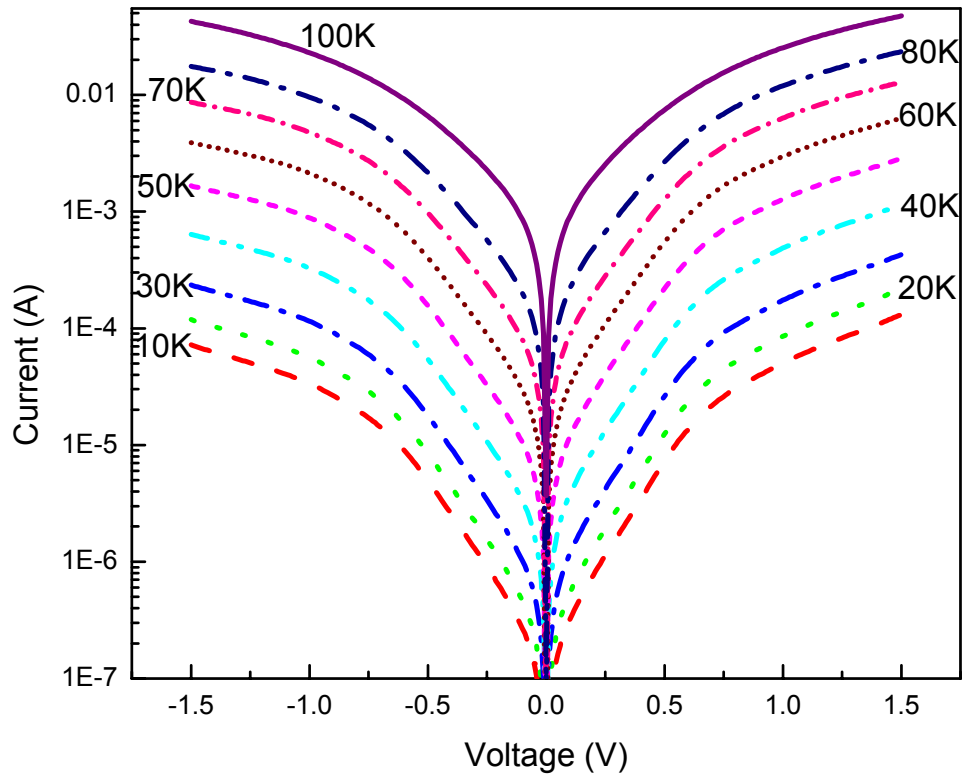


Figure 27. I-V Characteristics of Test Detector for Different Temperatures.

In order to measure the dark current without the background, the sample was carefully wrapped in aluminum foil to form a cold shield which blocks background radiation. In this case, only thermal excitation of the electrons at the prevailing temperature contributes to the current measured, which is defined as the dark current. The dark current measurements were plotted and shown in Figure 28.

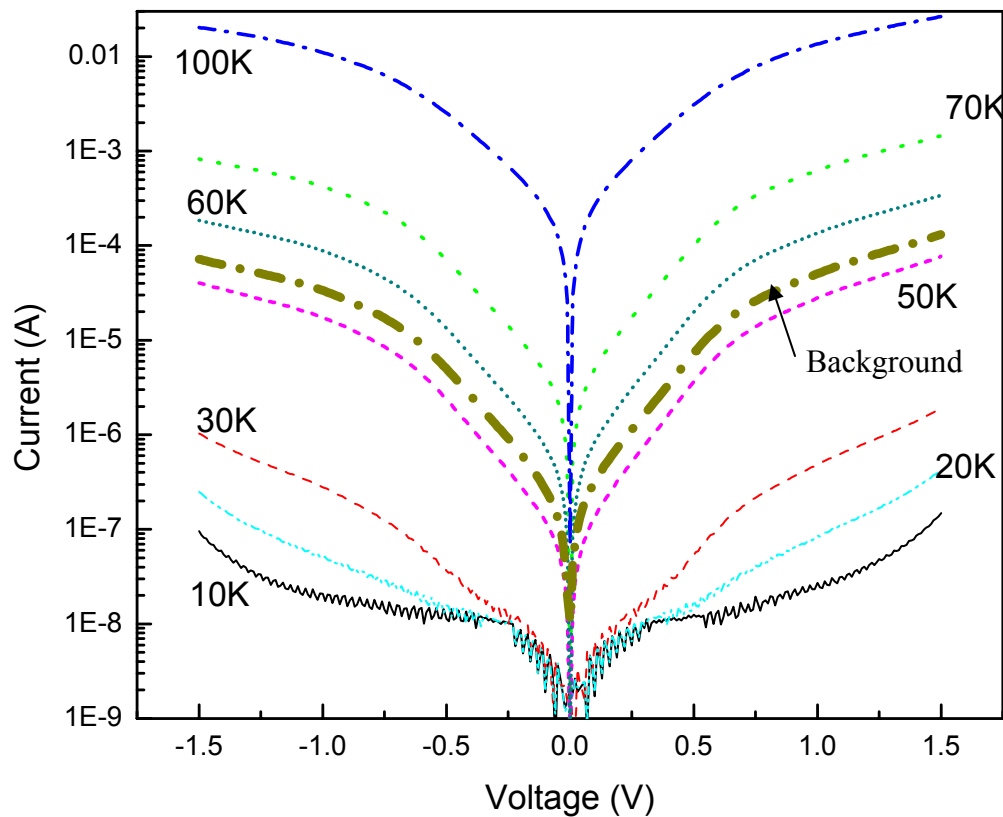


Figure 28. Dark Current Measurement.

Also plotted in the Figure 28 was the I-V curve at 10 K without the cold shield from Figure 27. It could be observed that this curve straddled between the dark currents at 50 K and 60 K. The significance of this is that the background infrared radiation actually contributed an equivalent amount of dark current as when the test detector was at a temperature of about 55K. This means that in an operational setting, there will be little use in lowering the temperature of the device below 55 K to improve the performance of the detector as the dark current caused by the background radiation had limited the performance of the detector at about 55 K. Any attempts would be wasted efforts as the background radiation would become the dominant noise factor. This is called the background limited infrared performance of the detector or BLIP. This measurement of BLIP performance at 55 K was consistent with that measured by Touse of the same

detector in an earlier thesis (Touse, 2003)

Another feature that could be observed from the dark current measurements of the test detector was the presence of periodic variations of the dark currents at low temperatures. These variations were not due to noise as otherwise they would be observed for higher temperatures. To look at these variations more clearly, Figure 29 was plotted to show the dark currents for the temperatures at 10 K, 20 K, 30 K and 50 K under negative bias. It can be seen that the periodic variations were present for temperatures up to 30 K, while from 50 K onwards, they were not observable.

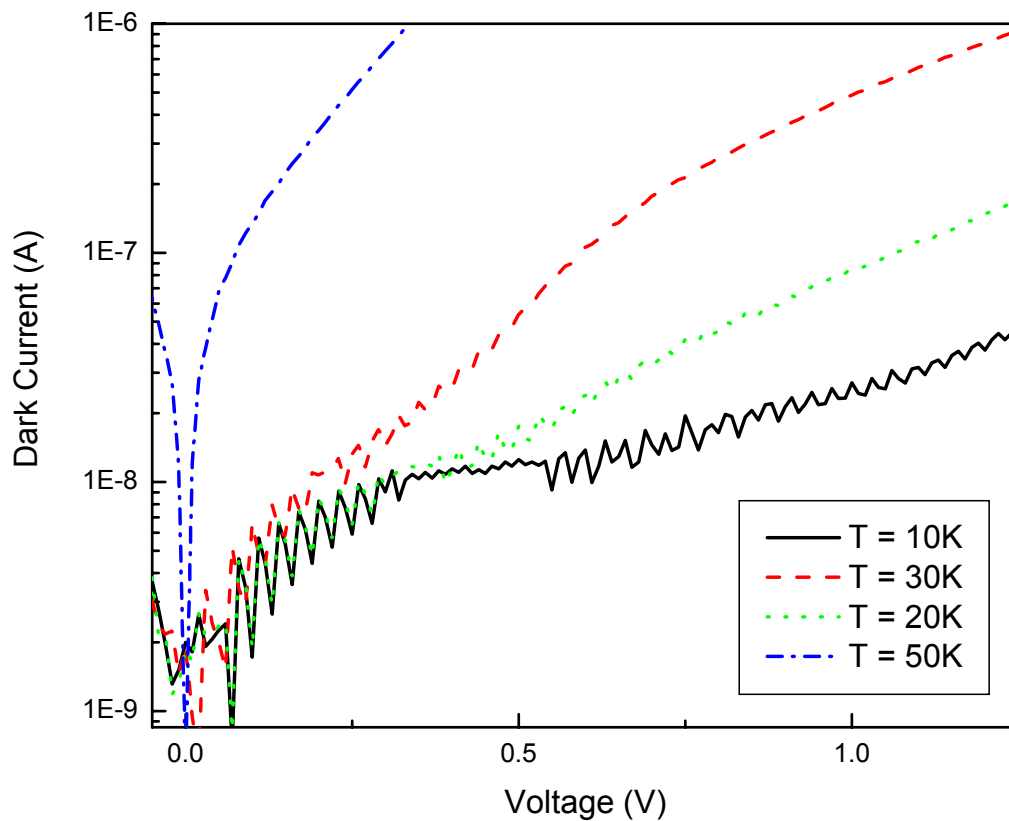


Figure 29. Periodic Dark Currents at Low Temperatures.

The periodic variations can be attributed to the negative differential conductance of the test detector at low temperatures (Levine, 1993). At these temperatures, there exist very little thermal excitation of the electrons to their excited states. As the bias voltage was increased, the energy bands of the quantum wells began to bend as shown in Figure 30 until the ground state in the conduction band of the well to the left of the right most well began to align with the excited state of the latter well so that electrons can tunnel through to produce a tunneling current. The sequential alignment of the ground states and the adjacent excited states to the right was the cause for the periodic nature of the variations. These variations were not evident at higher temperatures because of the dominant contribution to the dark current came from the thermionic emission.

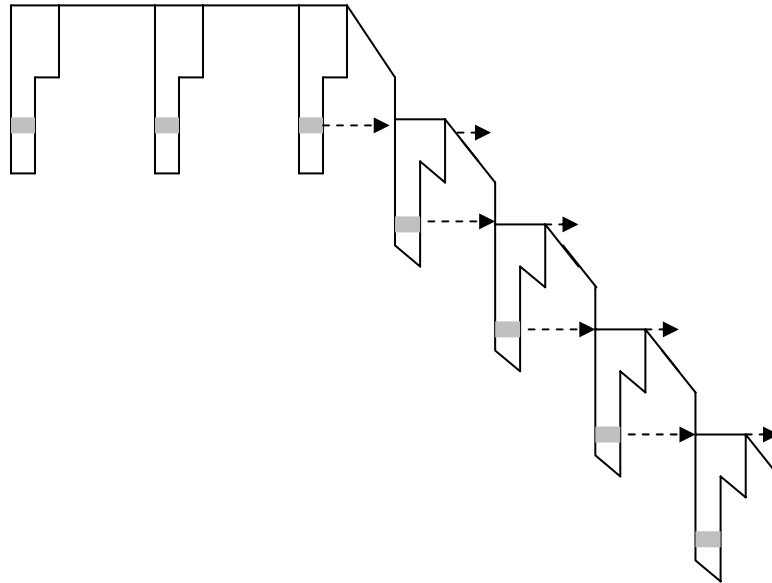


Figure 30. Periodic Variation of Dark Current due to Sequential Resonant Tunneling.

D. DETECTIVITY

The second and equally important figure-of-merit for IR detectors that have been constantly used as a key performance parameter for comparison is the D^* or normalized detectivity, which is defined as the Signal-to-Noise Ratio (SNR) out of a detector when 1 W of radiant power is incident on the detector with an area of 1 cm² and noise-equivalent bandwidth of 1 Hz (Deneriak, et al, 1996). Mathematically, it is represented by eq. (4.7).

$$D^* = \frac{\sqrt{A_d \Delta f}}{NEP} \quad (4.7)$$

NEP is the noise equivalent power or the radiant power incident on the detector that would yield a SNR of 1, and is related to the noise current and responsivity of the detector through eq. (4.8).

$$NEP = \frac{i_n}{R_{\text{det}}} \quad (4.8)$$

where i_n is the noise current of the detector which can have many components such as Johnson noise, Shot noise and Generation and Recombination noise, etc. R_{det} is the responsivity of the detector. Simply put, as its name imply, it is the equivalent signal power that would have been generated by the noise current. As the test detector used here is of the photoconductive type, the major contributor to the noise was the Generation and Recombination Noise. The noise current in this case would be given by eq. (4.9) (Choi, 1997).

$$i_{gr} = \sqrt{4eGI\Delta f} \quad (4.9)$$

where G is the optical gain and which is close to 1 for quantum well detectors (Levine, 1993), e is the electronic charge, while I is the total current flowing through the detector and Δf is the bandwidth which is usually taken as 1 Hz (Levine, 1993). Thus, the detectivity can be represented by eq. (4.10).

$$D^* = R_{\text{det}} \sqrt{\frac{A_D \Delta f}{4eGI\Delta f}} = R_{\text{det}} \sqrt{\frac{A_D}{4eI}} \left(\frac{\text{cm}\sqrt{\text{Hz}}}{\text{W}} \right) \quad (4.10)$$

The most practical form of the detectivity which is commonly used for comparison is the detectivity at Background Limited Infrared Performance or $D^*(\text{BLIP})$. This would be the best performance that any detector can achieve since there will be no way to eliminate the environmental conditions that the detectors will be exposed to. With the maximum responsivity of 1.022 A/W measured at a negative bias of 0.83V, the corresponding current through the detector can be obtained from Figure 29 to be substituted into eq. (4.10). At operating temperature of 10 K and bias of -0.83 V the background current was 2.19×10^{-5} A. In this case, the $D^*(\text{BLIP})$ was calculated to be $8.0 \times 10^9 \text{ cm}\sqrt{\text{Hz}}/\text{W}$. In addition, the detectivity of the detector at BLIP under different bias was also plotted in Figure 31. The reduction of detectivity at low bias is due to the decrease of responsivity of the detector.

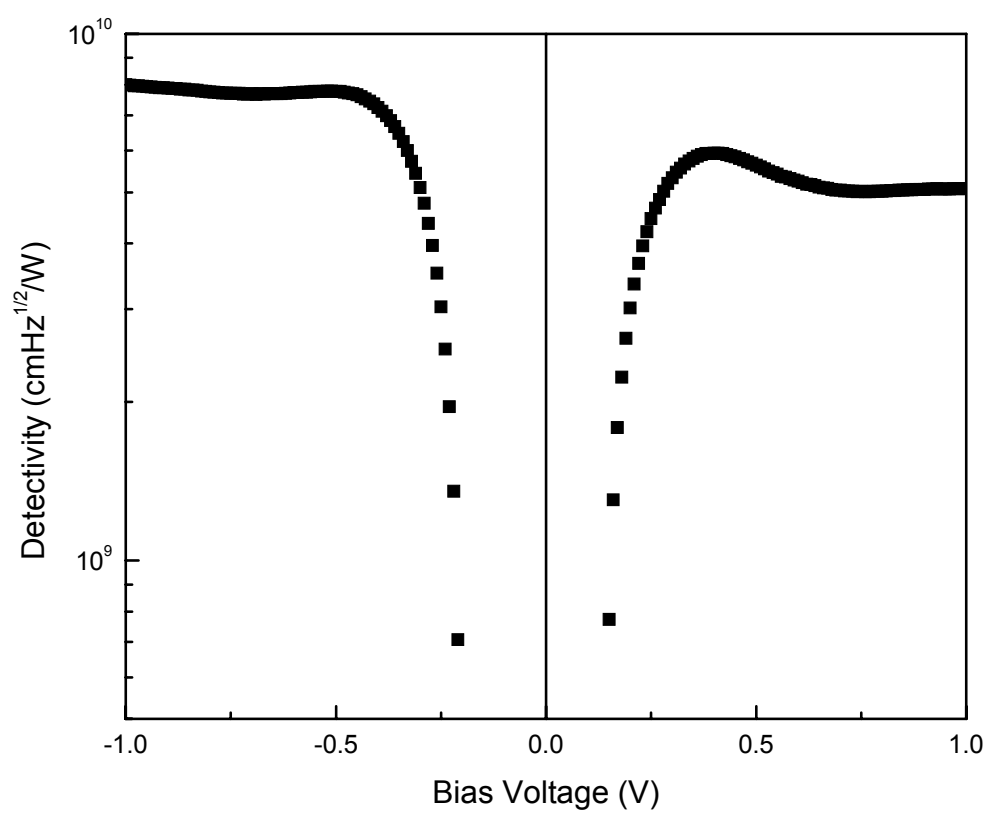


Figure 31. Detectivity (BLIP) of the Test Detector Under Different Bias Conditions.

THIS PAGE INTENTIONALLY LEFT BLANK

V. CONCLUSION

In this thesis, the performance of a step quantum well infrared photodetector was evaluated and analyzed. The QWIP, which comprised of 25 step wells, was originally designed to operate in both the NIR window and the FIR window to detect a laser spot of $1.06\ \mu\text{m}$ and provide IR imagery centered between $9.5\ \mu\text{m}$ to $10.5\ \mu\text{m}$ window. The focus of the thesis was to characterize detector response in the FIR to establish the performance as well as explore the tunability of the detection wavelength. The asymmetry of the quantum well was deliberately introduced to overcome selection rules to realize both band-to-band and intersubband transitions as well as to achieve tunability. As a consequence of the asymmetry, linear stark effect would be present and would cause the peaks in the FIR to be shifted as the electric field across the quantum well was varied.

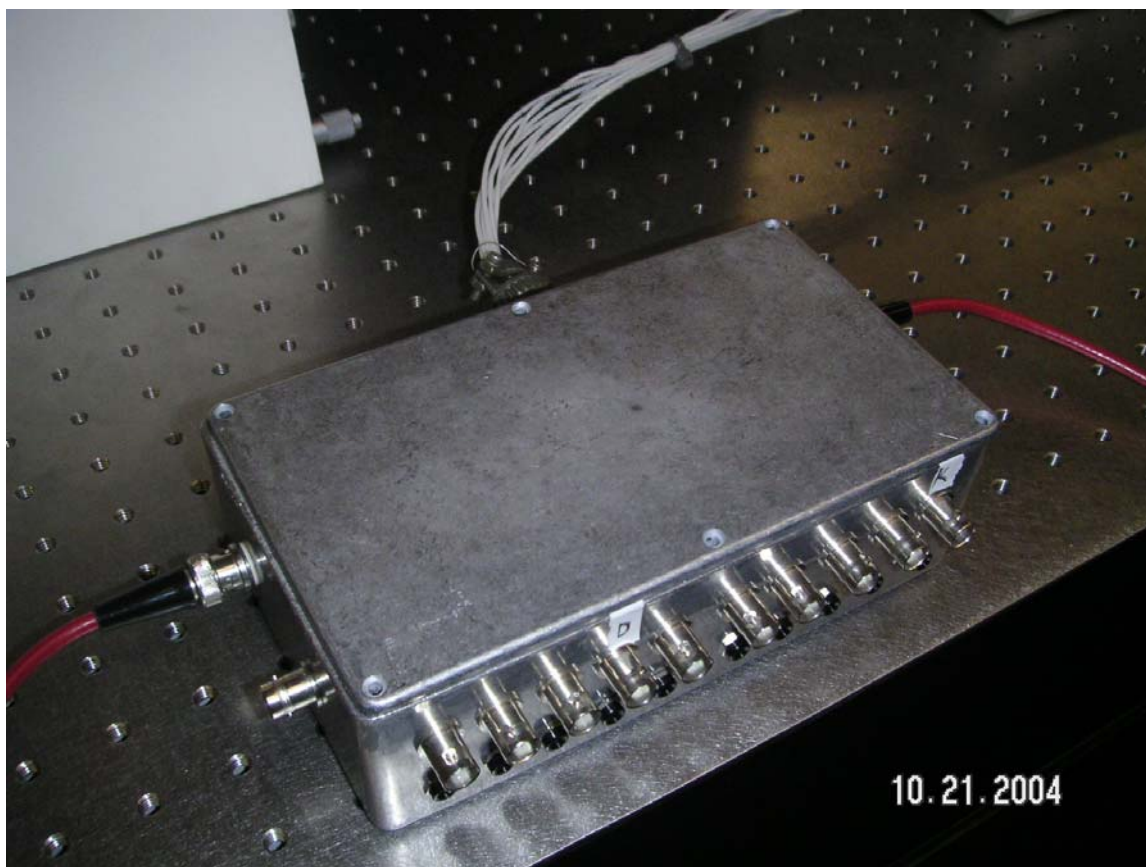
In the FIR, it was observed that as the bias voltage was increased from $-0.83\ \text{V}$ to $+0.81\ \text{V}$, the peak wavelength was red-shifted from $10.31\ \mu\text{m}$ to $10.62\ \mu\text{m}$. The equivalent shift in energy terms was $3.6\ \text{meV}$ which was very close to the theoretically predicted value of $3.45\ \text{meV}$. In the case of square quantum wells the equivalent shift is about $0.5\ \text{meV}$ (Harwitt, et al, 1987). The effective stark shift in response to the electric field was $0.21\ \text{meV/KVcm}^{-1}$. The maximum responsivity for the test detector was $1.022\ \text{A/W}$ at a peak wavelength of $10.32\ \mu\text{m}$ under a negative bias voltage of 0.83V . The detectivity, D^* , at background limited infrared performance was measured to be $8.0 \times 10^9\ \text{cm}\sqrt{\text{Hz}}/\text{W}$.

The IV characteristic for the test detector was also studied. The dark current of the detector at a temperature of $10\ \text{K}$ was $1.54 \times 10^{-8}\ \text{A}$, while background conditions produced a current of $2.19 \times 10^{-5}\ \text{A}$ at $10\ \text{K}$. With this information, it was found that the detector's background limited infrared performance occurred at about $55\ \text{K}$, which was consistent with that measured by Lantz in an earlier thesis.

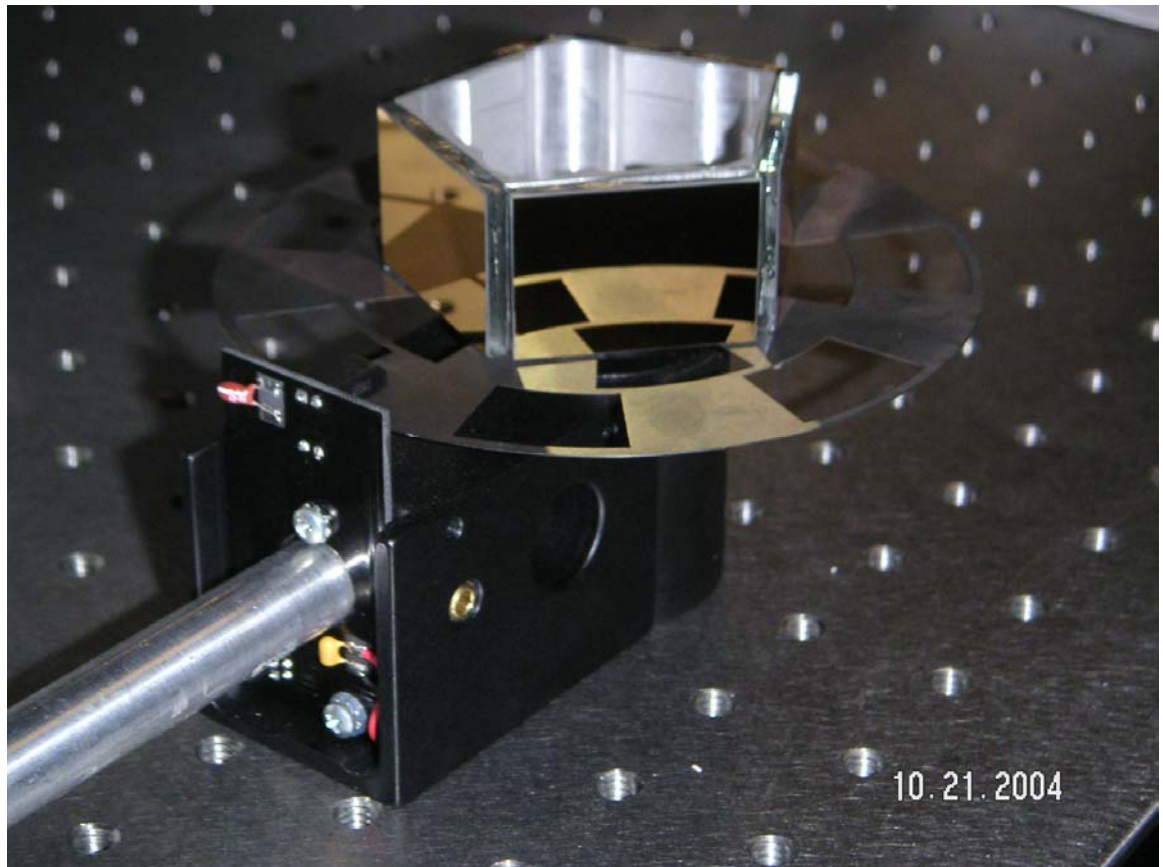
In conclusion, the test detector performed well in producing a relatively high responsivity of 1 A/W, and the tunability of the step quantum well had been measured and verified.

APPENDIX A : PICTURES OF THE JUNCTION BOX AND ROTATING MIRRORS

A. Picture of Junction Box for Application of Bias and Taking Measurements.



B. Picture of Rotating Platform with Mirrors Powered by Chopper Motors with Circular Slits for Feedback.



APPENDIX B : SPECIFICATION SHEETS

A. Specification Sheet for Reference Detector (70124)

70123-M
PYROELECTRIC DETECTOR
HEADS

Two Active Areas and Two Windows Types

We offer detector heads with 2 mm or 5 mm diameter detector active area and windows of either Thallium Bromiodide (KRS-5) or Calcium Fluoride (CaF_2). KRS-5 covers wavelengths from 0.6 to 50 micrometer, and CaF_2 covers 0.45 to 9 micrometers. Both detectors include a compensating preamplifier and both are carefully calibrated.

- The 70128/70364 and 70129/70365 have 2 mm diameter area useful for many laser or focused beam applications.
- The 70123/70362 and 70124/70363 have a 5 mm diameter detector element. The large area makes this detector useful for monitoring the output of monochromators or for applications where it is not possible to focus the radiation tightly.
- The 70123/70362 and 70128/70364 have CaF_2 windows.
- The 70124/70363 and 70129/70365 have KRS-5 windows.

Both detectors have oversize windows to prevent vignetting at high F numbers. However, some fall off of radiant energy will occur as the angle of incidence of radiation falling on the detector window gets more shallow (reflection losses increase with decreasing angles to the window surface).

Lithium Tantalate Elements

These detectors use lithium tantalate crystals in sealed housings to minimize the effects of air currents, humidity, ambient temperature and to provide long term stability. The crystals have a proprietary black coating to enhance the responsivity and minimize spectral response variations. The relative response of the blackened elements is essentially flat from below 0.2 micrometer to beyond 30 micrometers. The window material limits the spectral extent the responsivity. See Figure 2 for relative responsivities of the detector, CaF_2 and KRS-5.

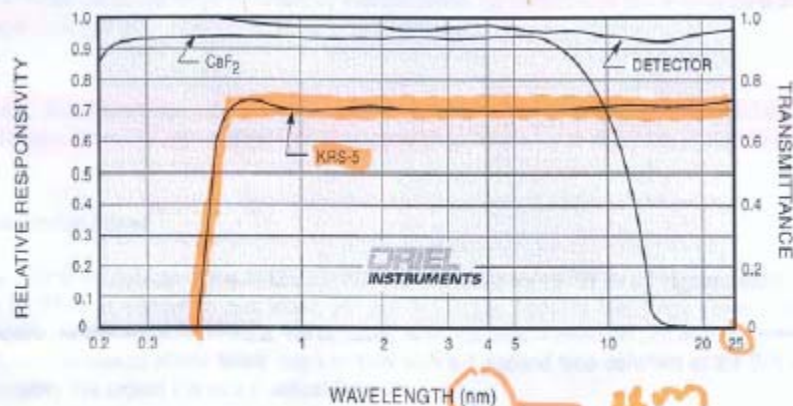
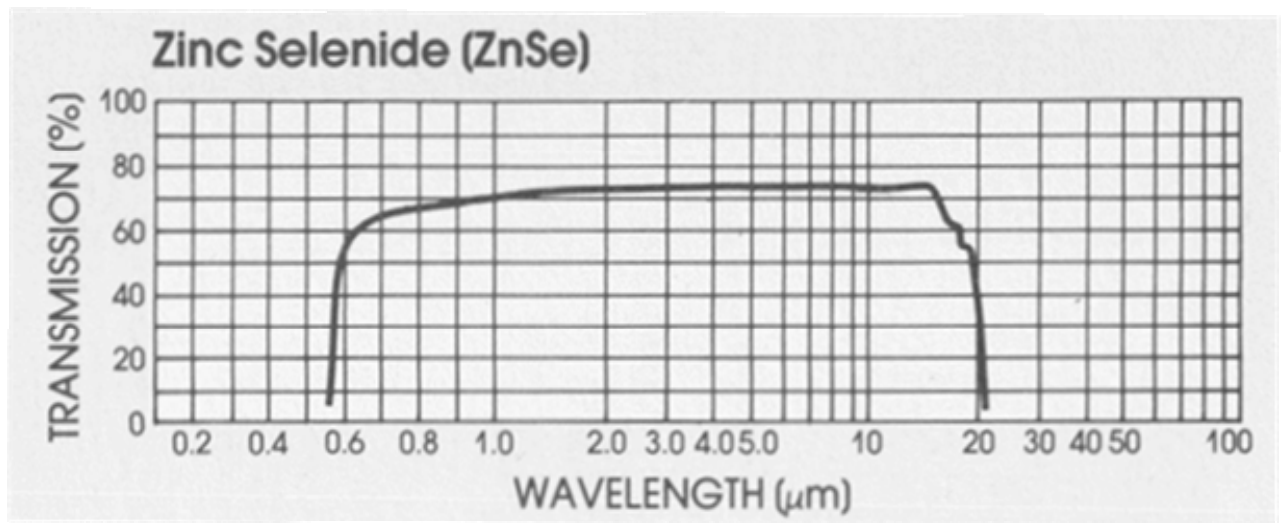


Fig. 2 Relative spectral response of blackened Lithium Tantalate detectors and transmission of KRS 5 and CaF_2 Windows

B. Transmittance Plot for Zinc Selenide



LIST OF REFERENCES

- Sarusi, G., *QWIP or Other Alternative for Third Generation Infrared Systems*, Infrared Physics & Technology, **44**, (2003).
- Harwit, A., Harris, J.S., *Observation of Stark Shifts in Quantum Well Intersubband Transitions*, Appl. Phys. Lett., **50**, p. 685, (1987).
- Yuh, P.F., Wang, K.L., *Optical Transitions in a Step Quantum Well*, J. Appl. Phys., **65**(11), pp. 4377-4379, (1989).
- Yuh, P.F., *Large Stark Effects for Transition from Local States to Global States in Quantum Well Structures*, IEEE J. Quantum Electron., **25**(7), pp. 1671–1674, (1989).
- Mii, Y.J., Karunasiri, R.P.G., Wang, K.L., Chen, M., Yuh, P.F., *Large Stark Shifts of the Local State Intersubband Transitions in Step Quantum Wells*, Appl. Phys. Lett., **56**(20), pp. 1986-1988, (1990).
- Martinet, E., Rosencher, E., Lu, F., Bois, Ph., Costard, E., Delaitre, S., *Switchable Bicolor (5.5-9.0 μ m) Infrared Detector Using Asymmetric GaAs/AlGaAs Multiquantum Well*, Appl. Phys. Lett., **61**(3), pp. 246-247, (1992).
- Wu, W.G., Chang, K., Jiang, D.S., Li, Y.X., Zheng, H.Z., Liu, H.C., *$\text{In}_x\text{Ga}_{1-x}\text{As}/\text{Al}_y\text{Ga}_{1-y}\text{As}/\text{Al}_z\text{Ga}_{1-z}\text{As}$ Asymmetric Step Quantum-well Middle Wavelength Infrared Detectors*, J. Appl. Phys., **90**(7), pp. 3437-3439, (2001).
- Dereniak, E.L., Boreman, G.D., *Infrared Detector and Systems*, John Wiley and Sons, Inc., p. 34, (1996).
- Levine, B. F., *Quantum-well Infrared Photodetectors*, J. Appl. Phys., **74**, (1993).
- Kasap, S.O., *Optoelectronics and Photonics, Principles and Practices*, Prentice Hall, p. 221, (2001).
- Haegel, N.M., *Semiconductors for Visible to Far-Infrared Detection*, Photodetectors and Fiber Optics, Academic Press, Chap 1, Sect. 6, p. 82, (2001).

Gunapala, S.D., Park, J.S., Sarusi, G., True-Lon Lin, Liu, J.K., Maker, P.D., Muller, R.E., Shott, C.A., Hoelter, T., *15- μ m 128 \times 128 GaAs/Al_xGa_{1-x}As Quantum Well Infrared Photodetector Focal Plane Array Camera*, IEEE Trans. Elec. Dev., **45**, (1997).

Touse, M.P., *Demonstration of a Near and Mid Infrared Detector using Multiple Step Quantum Wells*, Masters' Thesis, Naval Postgraduate School, Monterey, California, (2003).

Herdlick, B.E., *Computer Controlled Photodetector Characterization System (Design and Construction)*, Masters' Thesis, Naval Postgraduate School, Monterey, California, (2002).

Lantz, K.R., *Two-Color Photodetector Using an Asymmetric Quantum Well Structure*, Masters' Thesis, Naval Postgraduate School, Monterey, California (2002).

Hickey, T. R., *Temperature Dependence of Dark Current in Quantum Well Infrared Photodetectors*, Masters' Thesis, Naval Postgraduate School, Monterey, California, (2002).

Liboff, R.L., *Introductory Quantum Mechanics*, Addison Wesley, 4th ed., p. 92, (2003).

Choi, K.K., *The Physics of Quantum Well Infrared Photodetectors*, World Scientific Publishing Co., p. 20, p. 122, (1997).

Karunasiri, R.P.G., *Lecture Notes for PH4272 on QWIP*, (2004).

Mii, Y.J., Wang, K.L., Karunasiri, R.P.G., Yuh, P.F., *Observation of Large Oscillator Strengths for both 1 to 2 and 2 to 3 Intersubband Transitions of Step Quantum Wells*, Appl. Phys. Lett., **56**(11), pp. 1046-1048, (1990).

Karunasiri, R.P.G., Mii, Y. J., Wang, K.L., *Tunable Infrared Modulator and Switch Using Stark Shift in Step Quantum Wells*, IEEE Electron. Device Lett., **11**(5), p. 227, (1990).

Yuh, P.F., Wang, K.L., *Large Stark Effects for Transitions from Local States to Global States in Quantum Well Structures*, IEEE J. Quantum Electron., **25**(7), pp. 1671-1674, (1989).

Singh, *Physics of Semiconductors and their Heterostructures*, McGraw-Hill Book Co., pp. 184-185, (1993), cited in Lantz, K.R., Two-Color Photodetector using an Asymmetric Quantum Well Structure, Masters' Thesis, Naval Postgraduate School, Monterey, California (2002).

THIS PAGE INTENTIONALLY LEFT BLANK

INITIAL DISTRIBUTION LIST

1. Defense Technical Information Center
Ft. Belvoir, Virginia
2. Dudley Knox Library
Naval Postgraduate School
Monterey, California
3. Gamani Karunasiri
Naval Postgraduate School
Monterey, California
4. James Luscombe
Naval Postgraduate School
Monterey, California